DEVELOPMENTAL BIOLOGY

Tie2 activation promotes choriocapillary regeneration for alleviating neovascular age-related macular degeneration

Jaeryung Kim[1,2,3]*, Jang Ryul Park[4,5]*, Jeongwoon Choi[1,2], Intae Park[1,2], Yoonha Hwang[5,6], Hosung Bae[1,2], Yongjoo Kim[4,5], WooJhon Choi[5], Jee Myung Yang[2], Sangyeul Han[1], Tae-Young Chung[3], Pilhan Kim[5,6], Yoshiaki Kubota[7], Hellmut G. Augustin[8,9], Wang-Yuhl Oh[4,5†], Gou Young Koh[1,2†]

Choriocapillary loss is a major cause of neovascular age-related macular degeneration (NV-AMD). Although vascular endothelial growth factor (VEGF) blockade for NV-AMD has shown beneficial outcomes, unmet medical needs for patients refractory or tachyphylactic to anti-VEGF therapy exist. In addition, the treatment could exacerbate choriocapillary rarefaction, necessitating advanced treatment for fundamental recovery from NV-AMD. In this study, Tie2 activation by angiopoietin-2–binding and Tie2-activating antibody (ABTAA) presents a therapeutic strategy for NV-AMD. Conditional *Tie2* deletion impeded choriocapillary maintenance, rendering eyes susceptible to NV-AMD development. Moreover, in a NV-AMD mouse model, ABTAA not only suppressed choroidal neovascularization (CNV) and vascular leakage but also regenerated the choriocapillaris and relieved hypoxia. Conversely, VEGF blockade degenerated the choriocapillaris and exacerbated hypoxia, although it suppressed CNV and vascular leakage. Together, we establish that angiopoietin-Tie2 signaling is critical for choriocapillary maintenance and that ABTAA represents an alternative, combinative therapeutic strategy for NV-AMD by alleviating anti-VEGF adverse effects.

INTRODUCTION

Neovascular age-related macular degeneration (NV-AMD) is a leading cause of irreversible vision loss among elderly persons in developed countries (*1*). NV-AMD is characterized by the formation of choroidal neovascularization (CNV), an ingrowth of abnormal blood vessels from the choroid through Bruch's membrane into the subretinal pigment epithelium (RPE) or subretinal space (*2*). Throughout this ingrowth, abnormal leakages of fluids and bloods occur into the retina, causing vision distortion and loss of central vision (*2*, *3*). To treat neovascular eye diseases including NV-AMD, anti–vascular endothelial growth factor A (VEGF) therapy has largely been used based on the fact that an excessive production of VEGF from hypoxic cells in the retino-choroidal complex is critical in the pathogenesis and features of neovascular eye diseases (*3*, *4*). Nevertheless, intravitreal anti-VEGF therapy only temporarily suppresses CNV and its vascular leakage in NV-AMD, necessitating periodic and repeated administrations for several years (*5*). There have been controversies on the adverse effects of long-term and repetitive anti-VEGF therapy. Although some studies have reported that frequent, chronic anti-VEGF injection is effective and safe (*6*, *7*), others have had a long-standing concern that this long-term anti-VEGF therapy can arrest the normal repair processes in the NV-AMD and aggravate hypoxia and oxidative stress in the retino-choroidal complex, leading to RPE damage, photoreceptor degeneration, and permanent vision loss (*8*–*11*).

The choriocapillaris, the innermost layer of the choroid, is a specialized vascular structure in the eye that functions as the major blood supply for the outer retina including photoreceptors and the RPE (*12*). Together with hypoxia, oxidative stress and inflammation in the RPE (*2*), loss of the choriocapillaris, and subsequent reduction in blood supply have been postulated to be the main initial insults in the development of NV-AMD by making adjacent outer retinal layers hypoxic (*2*, *13*, *14*). Previous studies (*10*, *11*) revealed that VEGF is a critical regulator for maintaining the choriocapillaris in the adult eye. Therefore, an intensive VEGF blockade strategy would be detrimental to choriocapillary maintenance by preventing the trophic effect of VEGF, aggravating the initial insult that triggered NV-AMD. To avoid or relieve the adverse effects of anti-VEGF therapy on the maintenance of the choriocapillaris, RPE, and photoreceptors, a desirable aim is an alternative, combinative strategy that promotes adequate regeneration of the choriocapillary vascular network.

The angiopoietin (Angpt)–Tie2 system functions as a key regulator of vascular maturation and homeostasis (*15*). In accordance with this concept, vascular stabilization through Tie2 activation by vascular endothelial–phosphotyrosine phosphatase (VE-PTP) inhibition or COMP-Ang1 prevents vascular leakage from the CNV and lessens retinal edema (*16*, *17*). Tie2 activation also induces a healthy neovascularization without leakage and inflammation, which is a critical process for proper tissue regeneration (*18*). However, it is unknown whether Tie2 activation can induce regeneration of impaired choriocapillaris in NV-AMD, and a Tie2 activation strategy could be a potential therapeutic option for treating NV-AMD, especially for cases that are refractory or tachyphylactic to anti-VEGF

[1]Center for Vascular Research, Institute for Basic Science (IBS), Daejeon 34141, Republic of Korea. [2]Graduate School of Medical Science and Engineering, Korea Advanced Institute of Science and Technology (KAIST), Daejeon 34141, Republic of Korea. [3]Department of Ophthalmology, Samsung Medical Center, Sungkyunkwan University School of Medicine, Seoul 06351, Republic of Korea. [4]Department of Mechanical Engineering, KAIST, Daejeon 34141, Republic of Korea. [5]KI for Health Science and Technology (KIHST), KAIST, Daejeon 34141, Republic of Korea. [6]Graduate School of Nanoscience and Technology, KAIST, Daejeon 34141, Republic of Korea. [7]The Laboratory of Vascular Biology, School of Medicine, Keio University, Tokyo 160-8582, Japan. [8]European Center for Angioscience (ECAS), Medical Faculty Mannheim, Heidelberg University, Mannheim 68167, Germany. [9]Division of Vascular Oncology and Metastasis, German Cancer Research Center, DKFZ-ZMBH Alliance, Heidelberg 69121, Germany.
*These authors contributed equally to this work.
†Corresponding author. Email: gykoh@kaist.ac.kr (G.Y.K.); woh1@kaist.ac.kr (W.-Y.O.)

therapy. Also unknown are the roles of Angpt-Tie2 signaling in the maintenance of choriocapillary integrity.

Here, we demonstrate that the Angpt-Tie2 system is continuously required to maintain the integrity of adult choriocapillaris. Using our recently developed dual-functioning antibody, ABTAA (Angpt2-binding and Tie2-activating antibody) (*19*, *20*), we show that Tie2 activation by intravitreal administration of ABTAA confers crucial and multiple benefits including suppressions of the CNV and vascular leakage, choriocapillary regeneration, and relief of hypoxia surrounding the CNV. These results point to the potential for an alternative, combinative treatment for NV-AMD.

RESULTS

Impaired Angpt1-Tie2 signaling during adulthood leads to choriocapillary loss and visual impairment

To gain insight into the role of Angpt1-Tie2 signaling in the maintenance of the choriocapillaris, we first examined Tie2 levels in the choriocapillaris of adult humans, which were obtained from the healthy cadaveric donor eyes for corneal transplantations. Relatively high levels of Tie2 were detected in choriocapillary endothelial cells (ECs) in young adult humans (mean age, 30.8 years; range, 20 to 36 years; $n = 5$), but the Tie2 level and choriocapillary density were reduced in older individuals (mean age, 71.2 years; range, 65 to 84 years; $n = 5$) (Fig. 1, A to C). Thus, the reduction in Tie2 by the ageing process could be one of the contributing factors for the pathogenesis of NV-AMD. We also examined expressions of Tie2 and Angpt1 in adult choroid using *Tie2*-GFP (green fluorescent protein) and *Angpt1*-GFP reporter mice (*21*). Tie2 expression was highly enriched in ECs, but Angpt1 expression was highly enriched in $NG2^+$ perivascular cells surrounding choroidal vessels (fig. S1, A and B).

To investigate the role of Tie2 in the adult choriocapillaris, we generated a $Tie2^{i\Delta EC}$ mouse by crossing the $Tie2^{flox/flox}$ mouse (*22*) with the *VE-cadherin*-Cre-ER^{T2} mouse (*23*) and deleted Tie2 from ECs of the choriocapillaris from 8-week-old animals by tamoxifen administration (Fig. 1D). Cre-ER^{T2}–positive but flox/flox–negative mice among the littermates were defined as wild-type (WT) mice. Although the choriocapillaris has the largest blood flow by weight in all organs (*12*), a detailed morphologic and functional analysis of it is extremely difficult in mice. To overcome these limitations, we used a newly developed optical coherence tomography angiography (OCTA) method (*20*). This advanced method allows not only a non-invasive and detailed visualization of blood-perfused capillary vascular networks of retina and choroid but also temporal monitoring in the same mouse (*20*). We performed intravital OCTA on the same day and at 4 and 8 weeks after initiation of tamoxifen administration (Fig. 1C) and calculated the relative retinal and choroidal blood flow from en face images exhibiting the retinal and choroidal layer, respectively (fig. S2). Consistent with previous findings (*24*, *25*), no significant differences were found in the retinal blood flow between $Tie2^{i\Delta EC}$ mice and WT mice over the time points (Fig. 1, E to G). In contrast, the choroidal blood flow was reduced by 18.8 to 19.0% in $Tie2^{i\Delta EC}$ mice 4 and 8 weeks later, while it was unchanged in WT mice (Fig. 1, E, F, and H). Moreover, $CD144^+$ adherens junctions in the choriocapillary ECs were reduced by 25.2 and 46.0% in $Tie2^{i\Delta EC}$ mice compared with WT mice 8 weeks later (Fig. 1, I and J). To exclude the possibility of elevated intraocular pressure (IOP) as a cause of the reduced choroidal blood flow in the $Tie2^{i\Delta EC}$ mice (*25*), we adapted the microbeads-induced ocular hypertension model (*26*). Although IOP was elevated up to 15 to 20 mmHg in this model, no significant reduction of choroidal blood flow was detected (fig. S3, A to F).

Given that the choriocapillaris is a major vessel for supplying blood to the outer retina including photoreceptors, we analyzed the photoreceptor function in mice using electroretinography (ERG). Compared to WT mice, $Tie2^{i\Delta EC}$ mice showed marked attenuation of photopic b-wave by 39.3 to 44.8%, at a range of stimulus intensities from 0.4 to 2.2 log cd·s/m^2, indicating impairment of cone photoreceptors (Fig. 2, A, B, and D). Moreover, cone photoreceptor outer segment density was reduced by 41.4% in the outer retina of $Tie2^{i\Delta EC}$ mice (Fig. 2, G and H). On the other hand, no significant changes were observed in the function and the density of rod photoreceptors (Fig. 2, C, E to G, and I). In addition, differences in opsin and rhodopsin protein expressions of retinas of $Tie2^{i\Delta EC}$ and WT mice were validated. In comparison with those of WT mice, retinas of $Tie2^{i\Delta EC}$ mice displayed reduced expression of opsin by 51.6% (Fig. 2, J and K). However, the rhodopsin level was not different between $Tie2^{i\Delta EC}$ and WT mice (Fig. 2, J and L). To confirm these findings, we examined whether the $Tie2^{i\Delta EC}$ mice has the mutations associated with photoreceptor degeneration including cng3, abca4, and pde6b (the rd1 mouse). The mice carried none of these mutations, suggesting that the photoreceptor degeneration in the $Tie2^{i\Delta EC}$ mice is caused by loss of the choriocapillaris and reduced blood supply.

To determine the role of Angpt1 in choriocapillaris maintenance during adulthood, we generated an $Angpt1^{i\Delta/\Delta}$ mouse by crossing the $Angpt1^{flox/flox}$ mouse (*27*) with the *ubiquitin*-Cre-ER^{T2} mouse. Similar to $Tie2^{i\Delta EC}$ mice, $Angpt1^{i\Delta/\Delta}$ mice also showed a gradual decrease in the choroidal blood flow by 22.2 to 23.7% during the follow-up period and reduced adherens junctions in choriocapillaris compared to those of WT mice (fig. S4, A to G). Moreover, cone photoreceptor density and photopic b-wave amplitude were also reduced in $Angpt1^{i\Delta/\Delta}$ mice (fig. S5, A to I). These findings indicate that Angpt1-Tie2 signaling is indispensable for maintenances of the choriocapillaris and cone photoreceptors.

Tie2 depletion during adulthood exacerbates CNV formation and suppresses choriocapillary regeneration surrounding the CNV lesions

These findings led us to ask whether *Tie2* deletion worsens the pathogenesis of NV-AMD. To answer this question, we used a mouse model of laser-induced CNV that mimics human NV-AMD (*28*), with some modifications (*16*), although it is not fully consistent with the pathogenesis of human NV-AMD. We deleted *Tie2* in ECs by tamoxifen administration to 8-week-old $Tie2^{i\Delta EC}$ mice, performed laser photocoagulation on retinas to rupture the RPE and Bruch's membrane at 12 weeks, and performed intravital OCTA at 7 days (D7) after laser injury and at D14, D21, and D35 (Fig. 3A). The relative volumes of CNV and the avascular space surrounding the site of laser injury were calculated from en face images exhibiting the outer retinal and choroidal layers, respectively.

There was a moderate reduction in CNV volume in the outer retinas of WT mice, but those of $Tie2^{i\Delta EC}$ mice showed some increase in CNV volume (Fig. 3, B to D). Compared with D7, *Tie2* depletion increased the avascular volume in choroids by 16.7, 14.0, and 29.5% at D14, D21, and D35, respectively. On the other hand, choroids of WT mice showed a reduction in the avascular volume by 20.6, 26.8, and 37.4%, respectively (Fig. 3, B, C, and E). These findings indicate that *Tie2* deletion exacerbated CNV formation

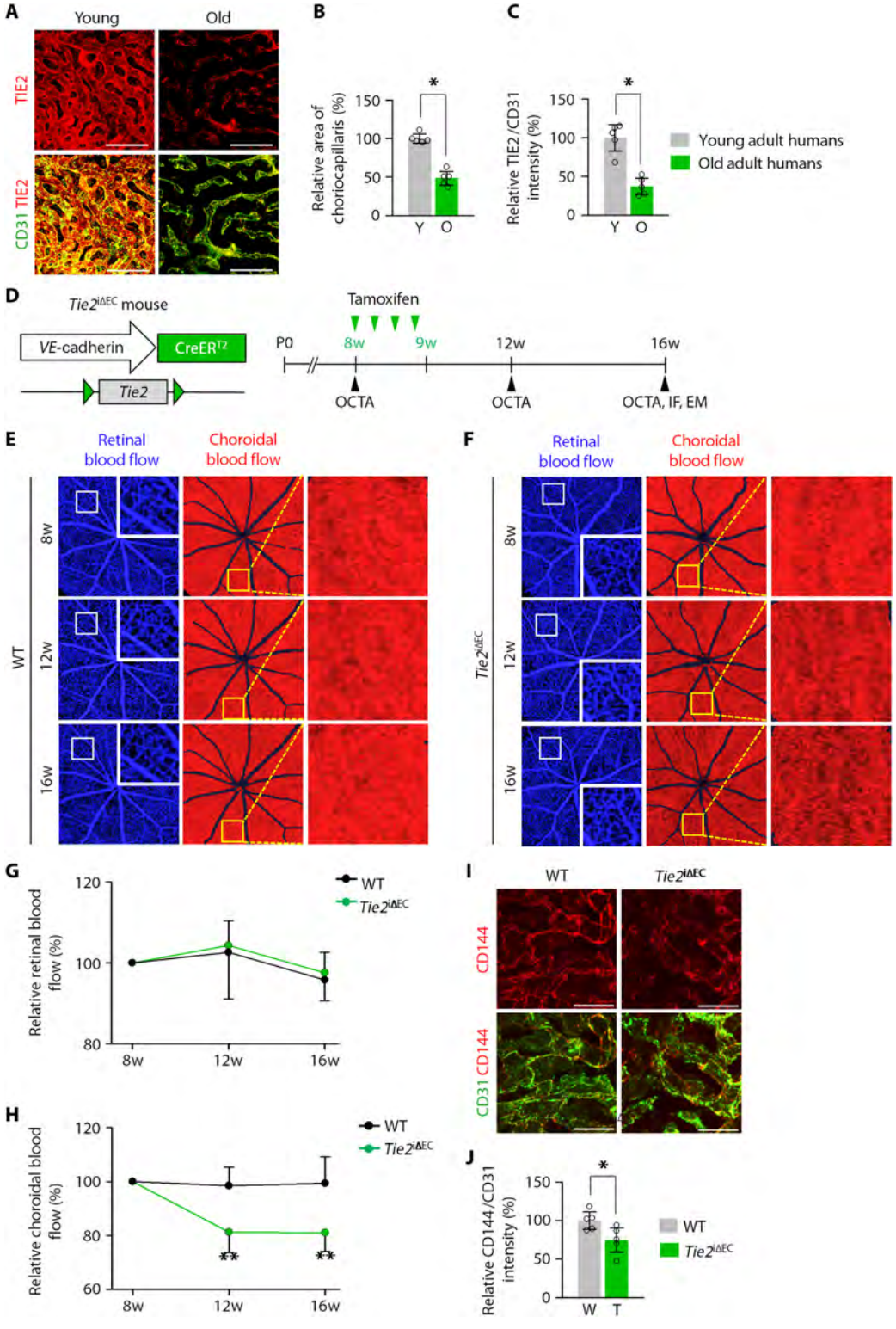

Fig. 1. *Tie2* deletion in adult ECs leads to damage and loss of choriocapillaris. (**A** to **C**) Images and comparisons of density and TIE2 intensity of $CD31^+$ choriocapillaris in healthy young adult (20 to 36 years old; Y) and old adult (65 to 84 years old; O) human subjects. Error bars represent means ± SD. Each group, $n = 5$. $^*P < 0.05$ versus Young by Mann-Whitney *U* test. Scale bars, 75 μm. (**D**) Diagram of schedule for EC-specific depletion of *Tie2* in 8-week-old mice and intravital OCTA at 8, 12, and 16 weeks (w) of age using $Tie2^{i\Delta EC}$ mice. (**E** and **F**) En face OCT angiograms showing retinal blood flow (left) and choroidal blood flow (middle) acquired by longitudinal OCTA imaging of eyes. Each area marked by a white box is magnified in the corner. Each area marked by a yellow box is magnified on the right panel. (**G** and **H**) Temporal changes in relative retinal (G) and choroidal (H) blood flow. Error bars represent means ± SD. Each group, $n = 10$. $^{**}P < 0.005$ versus WT by unpaired Student's *t* test. (**I** and **J**) Images and comparison of CD144 intensity in $CD31^+$ choriocapillaris. Error bars represent means ± SD. Each group, $n = 5$. $^*P < 0.05$ versus WT by Mann-Whitney *U* test. Scale bars, 20 μm.

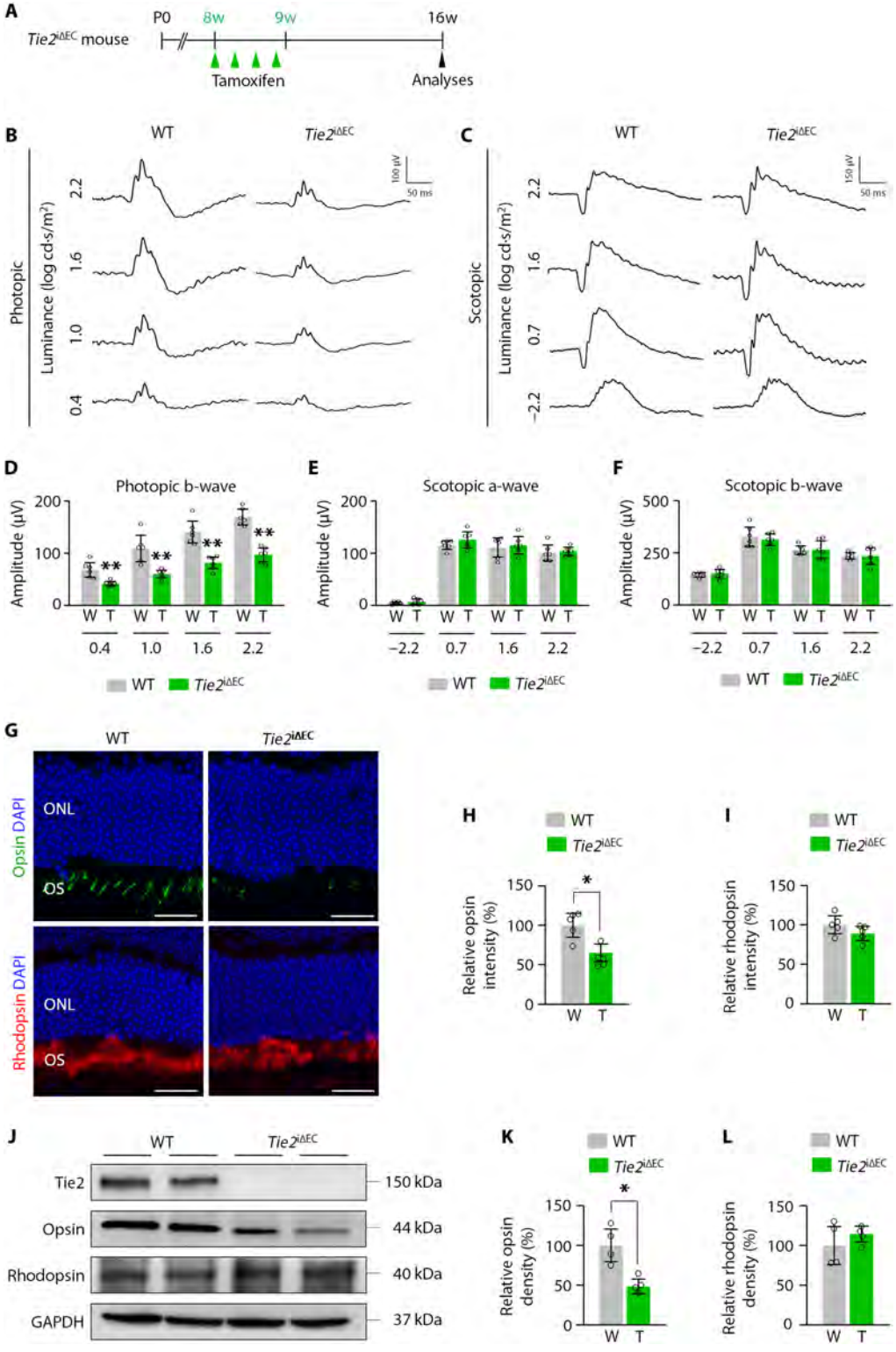

Fig. 2. Loss of cone photoreceptor and subsequent visual impairment in EC-specific *Tie2*-depleted mice. (**A**) Diagram for EC-specific depletion of *Tie2* in 8-week-old mice and analyses 2 months later using *Tie2*$^{i\Delta EC}$ mice. (**B** and **C**) Representative wave responses of ERG in photopic (B) and scotopic (C) conditions. (**D**) Comparisons of b-wave amplitude in photopic condition. Error bars represent mean ± SD. Each group, $n = 6$. $^{**}P < 0.005$ versus WT by Mann-Whitney *U* test. (**E** and **F**) Comparisons of a- and b-wave amplitudes in scotopic condition. Error bars represent mean ± SD. Each group, $n = 6$. (**G** to **I**) Expression of opsin and rhodopsin in photoreceptor layer. Error bars represent mean ± SD. Each group, $n = 6$. $^{*}P < 0.05$ versus WT by Mann-Whitney *U* test. Scale bars, 20 μm. ONL, outer nuclear layer; OS, outer segments of photoreceptor cells; DAPI, 4′,6-diamidino-2-phenylindole. (**J** to **L**) Immunoblot detection of opsin and rhodopsin proteins. Densitometric analyses of the relative level of opsin and rhodopsin are shown. Each group, $n = 4$. $^{*}P < 0.05$ versus WT by Mann-Whitney *U* test. GAPDH, glyceraldehyde-3-phosphate dehydrogenase.

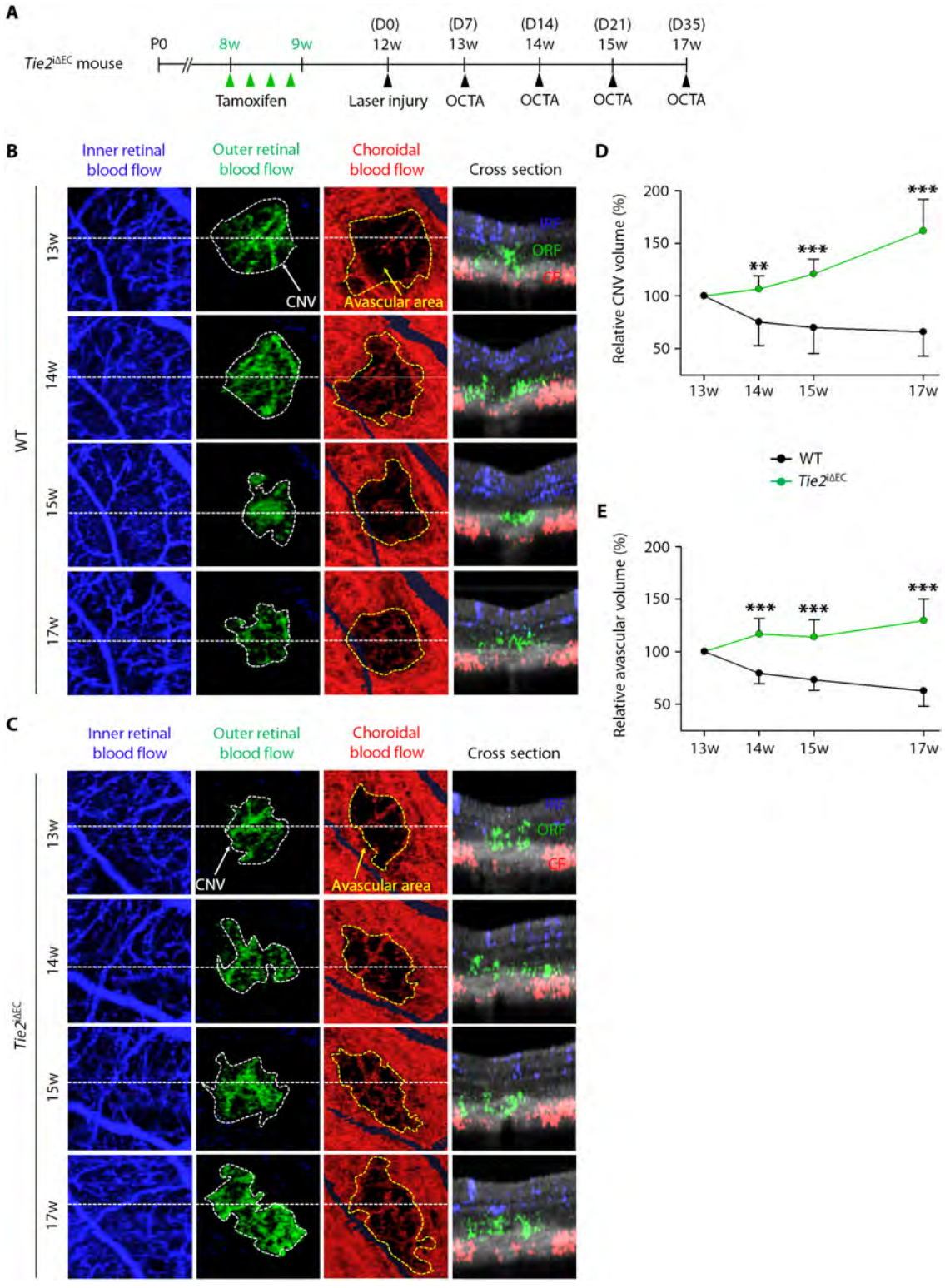

Fig. 3. *Tie2* deletion in adult ECs exacerbates CNV formation and hinders regeneration of choriocapillaris surrounding the CNV lesions. (**A**) Diagram of schedule for EC-specific depletion of *Tie2* in 8-week-old mice, induction of CNV after 4 weeks (D0), and intravital OCTA at D7, D14, D21, and D35 using *Tie2*$^{i\Delta EC}$ mice. (**B** and **C**) En face OCT angiograms and selected cross-sectional OCT angiograms of the locations indicated by white dotted lines showing inner retinal blood flow (blue), outer retinal blood flow (green), and choroidal blood flow (red) acquired by longitudinal OCTA imaging of eyes. En face angiogram of the outer retina showing the CNV (area demarcated by the white dotted boundary) and the choroid with avascular space (area demarcated by the yellow dotted boundary) surrounding the CNV. (**D** and **E**) Temporal changes in relative CNV volume (D) and avascular volume surrounding the site of laser photocoagulation (E). Error bars represent means ± SD. Each group, $n = 10$. $^{**}P < 0.005$, $^{***}P < 0.001$ versus WT by unpaired Student's *t* test.

and led to choriocapillary regression in the laser-induced CNV model.

ABTAA suppresses CNV and vascular leakage

To investigate the therapeutic effect of Tie2 activation on NV-AMD, ABTAA (5 μg each) was intravitreally administered to mice at D1 as a prevention phase (Fig. 4A). As a control or for comparison, Fc or VEGF-Trap (5 μg each) was administered in the same manner as that for the mice (Fig. 4A). To recapitulate a clinical scenario, the same treatments were performed at D7 as for a treatment phase (Fig. 4E). CNV volumes of the RPE-choroid-sclera flat mounts were calculated in both phases at D14. Consistent with a previous report (*29*), VEGF-Trap effectively reduced CNV volume by 63.0% (prevention phase; Fig. 4, B and C) and induced CNV regression by 64.4% (treatment phase; Fig. 4, F and G) compared with Fc. ABTAA similarly attenuated CNV volume (64.1%) in the prevention phase and induced CNV regression (65.3%) in the treatment phase (Fig. 4, B, C, F, and G). Combined fluorescein angiography (FA) and indocyanine green angiography (ICGA) enabled us to measure vascular leakage at the neovessels around the laser injury site. Compared with Fc, both VEGF-Trap (52.8 and 37.0%) and ABTAA (44.3 and 38.3%) similarly suppressed vascular leakage in both phases (Fig. 4, B, D, F, and H). Notably, the Fc-treated group showed no significant difference in vascular leakage between D6 and D14 in the treatment phase, but VEGF-Trap and ABTAA markedly reduced vascular leakage (45.6 and 50.0%, respectively) (Fig. 4, F and H). Thus, the magnitude of the suppression of CNV and vascular leakage was quantitatively indistinguishable between VEGF-Trap and ABTAA in the mouse model of laser-induced CNV.

ABTAA-induced Tie2 activation regenerates the choriocapillaris, leading to reduction of the avascular space surrounding the CNV lesions

To examine the effect of ABTAA-induced Tie2 activation on choriocapillary regeneration in the avascular space surrounding the site of laser injury from the initial period of CNV formation, we performed intravitreal injection of Fc, VEGF-Trap, or ABTAA (5 μg each) into mice at D1 (fig. S6A). Intravital OCTA was performed at D7, D14, D21, and D35 (fig. S6A), and the relative avascular volume surrounding the site of laser injury was calculated from en face images exhibiting the choroidal layer. There was a slight reduction in the avascular volume in choroids treated with Fc, whereas ABTAA gradually but markedly reduced the avascular volume by 26.9, 34.2, and 38.6% at D14, D21, and D35, respectively (fig. S6, B, D, and E). In contrast, VEGF-Trap somewhat increased the avascular volume by 35.9, 28.3, and 47.5% at D14, D21, and D35, respectively (fig. S6, B, C, and E).

To determine the effect of ABTAA on choriocapillary regeneration after establishment of CNV, we intravitreally administered Fc, VEGF-Trap, or ABTAA (5 μg each) to mice at D7, and intravital OCTA was performed at D6, D14, D21, and D35 (Fig. 5A). Similar to the results in the prevention phase, a slight reduction in the avascular volume was observed in choroids treated with Fc. Choroids in ABTAA-treated eyes showed serial and profound reduction in the avascular volume by 30.1, 36.4, and 37.0% at D14, D21, and D35, respectively (Fig. 5, B, D, E). However, choroids in VEGF-Trap–treated eyes showed an avascular volume increase by 11.4, 16.0, and 18.1% at D14, D21, and D35, respectively (Fig. 5, B, C, and E). Overall, these findings indicate that ABTAA promotes regeneration of the choriocapillaris, while VEGF-Trap led to choriocapillary regression in the laser-induced CNV model.

ABTAA forms a complex with Angpt2 and Tie2 in the mouse CNV model

To investigate further how intravitreal ABTAA exerts therapeutic effects on NV-AMD, we then examined vitreal levels of Angpt2 and expression of Angpt2 and Tie2 in ECs of the CNV after laser photocoagulation. Vitreal Angpt2 concentration had increased 1.8-fold at D1 after laser injury and further increased by 2.1- to 2.2-fold at D3 and D5 (fig. S7, A and B), which is consistent with what is seen in patients with NV-AMD (*30*). The source of the increased Angpt2 was likely the diseased ECs because high expression of Angpt2 was selectively confined to the ECs of the CNV (fig. S7, C and D). The administered ABTAA was highly detectable in the Tie2-expressing ECs of the CNV (fig. S7, E to G). These findings imply that ABTAA binds to Angpt2 in the vitreal cavity and that this complex leads to binding, clustering, and activation of Tie2 by forming the triple complex of ABTAA-Angpt2-Tie2 (*19*) in ECs of the CNV and choriocapillaris. Meanwhile, no differences in the relative volumes of CNV and the avascular space surrounding the site of laser injury were found between the ABTAA-treated eye and the Fc-treated eye in the *Tie2*$^{i\Delta EC}$ mice (fig. S8, A to E), indicating that the action of ABTAA was mediated entirely through Tie2.

ABTAA alleviates hypoxia and favorably alters gene expression profiles in CNV lesions and the surrounding RPE-choroid complex

To address the beneficial effects of vascular alterations induced by ABTAA, we analyzed changes in hypoxia and hypoxia-related gene expression profiles at the CNV area and the surrounding RPE-choroid complex. Intravitreal administration of Fc, VEGF-Trap, or ABTAA (5 μg each) was performed in mice at D1, and the extent of hypoxia was measured by pimonidazole staining at D4 (Fig. 6A). ABTAA reduced the hypoxic area by 41.2% compared with Fc, whereas VEGF-Trap increased the hypoxic area by 32.4% (Fig. 6, B and C). RNA sequencing (RNA-seq) analysis of CNV lesions and surrounding tissues collected by laser capture microdissection revealed a markedly different pattern in response to ABTAA compared to the response to VEGF-Trap (fig. S9, A and B). In particular, the specific genes related to hypoxia were up-regulated by VEGF-Trap, whereas they were down-regulated by ABTAA (fig. S9C). Gene set enrichment analysis (GSEA) also identified that VEGF-Trap resulted in enrichment of genes up-regulated under hypoxic conditions in comparison to ABTAA (fig. S9D). In addition, differentially expressed genes (DEGs) in each condition (adjusted $P < 0.05$) were subjected to ingenuity pathway analysis (IPA) to allow for interpretation of the details associated with disease and biological function. Most hypoxia-induced terms were significantly enriched by VEGF-Trap, with up-regulation of terms related to cell death and apoptosis and suppression of terms related to cell proliferation, migration, and movement (fig. S9E and table S1). In contrast, ABTAA relieved the adverse effects of VEGF-Trap such as cell death and apoptosis and specifically suppressed cell death of retinal cells and apoptosis of RPE cells (fig. S9F and table S1). In addition, ABTAA promoted sprouting angiogenesis, cell movement, and viability (fig. S9F and table S1), implying that ABTAA-induced regeneration of the choriocapillaris facilitated the relief of hypoxia to provide a favorable microenvironment in the RPE and choroidal tissues of NV-AMD.

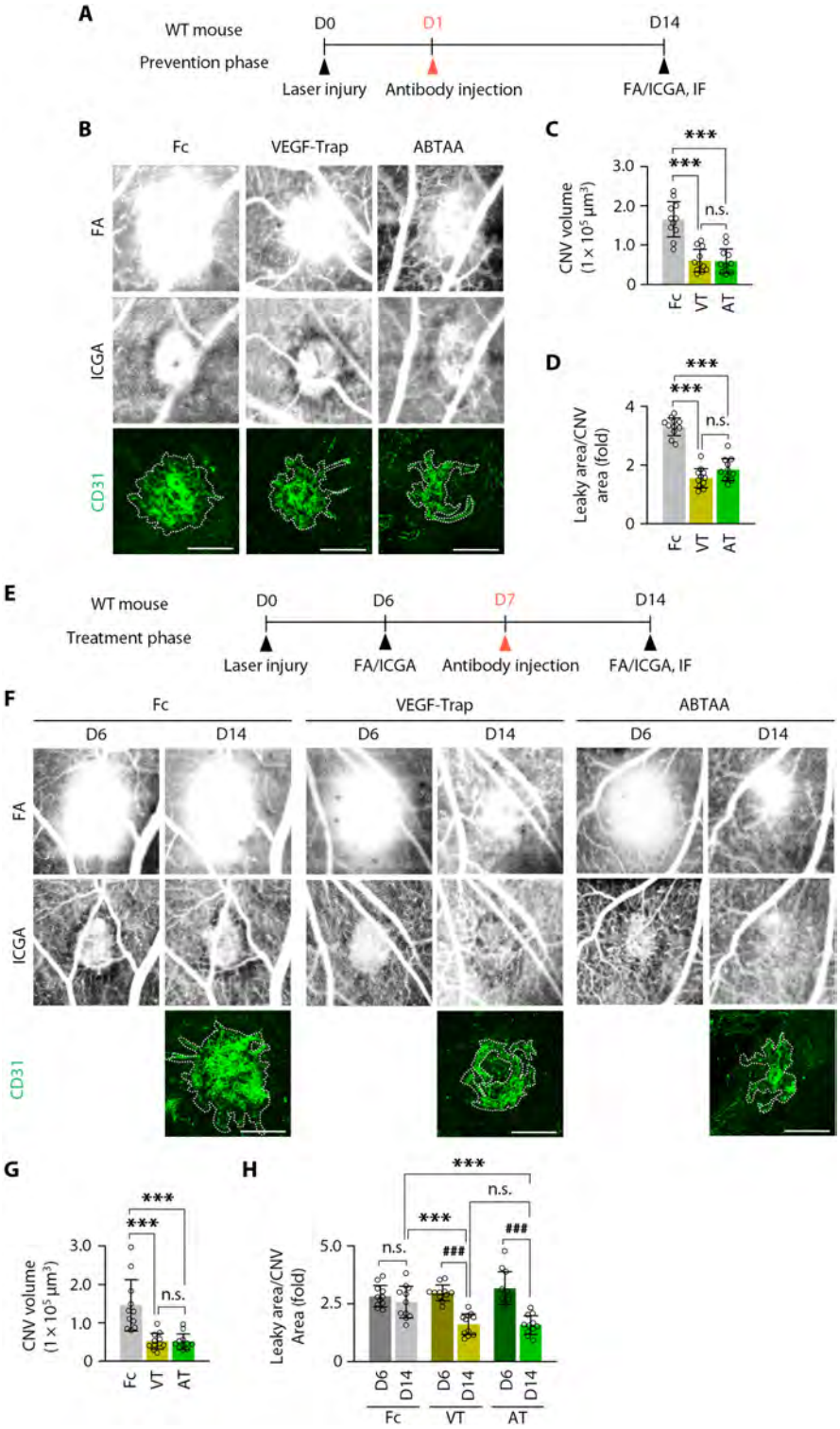

Fig. 4. ABTAA inhibits CNV formation and leads to CNV regression and vascular leakage suppression. (**A** and **E**) Diagram of schedule for induction of CNV at D0; intravitreal administration of Fc, VEGF-Trap, or ABTAA (5 μg each) at D1 (prevention phase) or D7 (treatment phase); and their analyses at D6 (treatment phase) and/or D14 (both phases). (**B** and **F**) Images of late-phase FA to detect vascular leakage surrounding the site of laser injury and ICGA and CD31 staining of RPE-choroid-sclera flat mounts to quantify the extent of CNV at D14 (both phases). (**C** and **G**) Comparisons of CNV volumes calculated as total $CD31^+$ volume at the site of laser photocoagulation. Error bars represent means ± SD. Each group, $n = 11$. $^{***}P < 0.001$ by one-way analysis of variance (ANOVA) followed by Student-Newman-Keuls post hoc test. (**D** and **H**) Comparisons of leaky areas around CNV calculated as the total measured hyper-fluorescent areas in FA images divided by the total measured CNV areas in ICGA images. Error bars represent mean ± SD. Each group, $n = 11$. $^{***}P < 0.001$ by one-way ANOVA followed by Student-Newman-Keuls post hoc test; $^{\#\#\#}P < 0.001$ by paired Student's *t* test. VT, VEGF-Trap; AT, ABTAA; n.s., not significant. Scale bars, 100 μm.

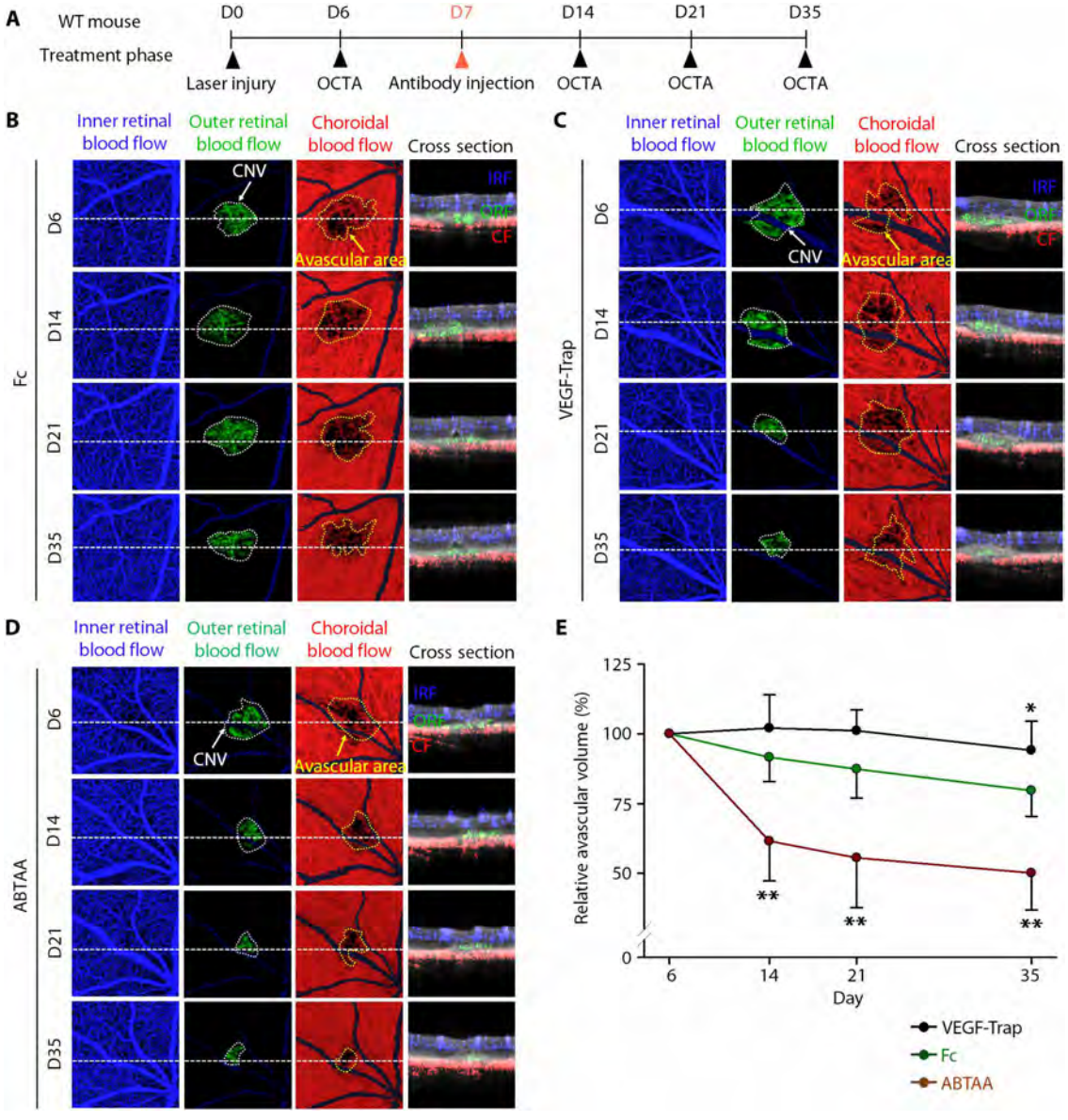

Fig. 5. ABTAA promotes regeneration of choriocapillaris surrounding the site of laser photocoagulation in the treatment phase. (**A**) Diagram of schedule for induction of CNV at D0, intravitreal administration of Fc, VEGF-Trap, or ABTAA (5 μg each) at D7 and intravital OCTA at D6, D14, D21, and D35 (treatment phase). (**B** to **D**) En face OCT angiograms and selected cross-sectional OCT angiograms of the locations indicated by white dotted lines showing inner retinal blood flow (blue), outer retinal blood flow (green), and choroidal blood flow (red) acquired by longitudinal OCTA imaging of eyes treated with Fc, VEGF-Trap, and ABTAA. En face angiogram of the outer retina showing the CNV (area demarcated by the white dotted boundary) and the choroid with the avascular space (area demarcated by the yellow dotted boundary) surrounding the CNV. (**E**) Temporal changes in relative avascular volumes surrounding the site of laser photocoagulation. Error bars represent means ± SD. Each group, $n = 11$. $^{*}P < 0.05$, $^{**}P < 0.005$ versus Fc by one-way ANOVA followed by Student-Newman-Keuls post-test.

DISCUSSION

In this study, we demonstrate that Angpt-Tie2 signaling is critical for maintaining the adult choriocapillaris. Impairment of this system leads to choriocapillary loss, a major causative event in NV-AMD (*2*, *13*). The most intriguing finding of this study is that ABTAA-induced Tie2 activation not only inhibited CNV with suppression of vascular leakage but also promoted regeneration of the choriocapillary vascular network, which is the critical step for fundamental recovery of NV-AMD (Fig. 6D). The regenerated choriocapillary vasculature subsequently alleviates hypoxia, leading to a favorable transition of the CNV microenvironment to prevent recurrence of NV-AMD. Thus, Tie2 activation by ABTAA represents an alternative, combinative therapeutic strategy for treating patients with NV-AMD with alleviation of the adverse effects that can arise from long-term treatment with VEGF blockade.

AMD is subdivided into two types: dry AMD and NV-AMD. For the past decades, impairment of the RPE has been considered as a principal player in the development of dry AMD (*31*). Dry AMD results from a gradual loss of RPE cells and the accumulation of drusenoid deposits, subsequently inducing photoreceptor degeneration

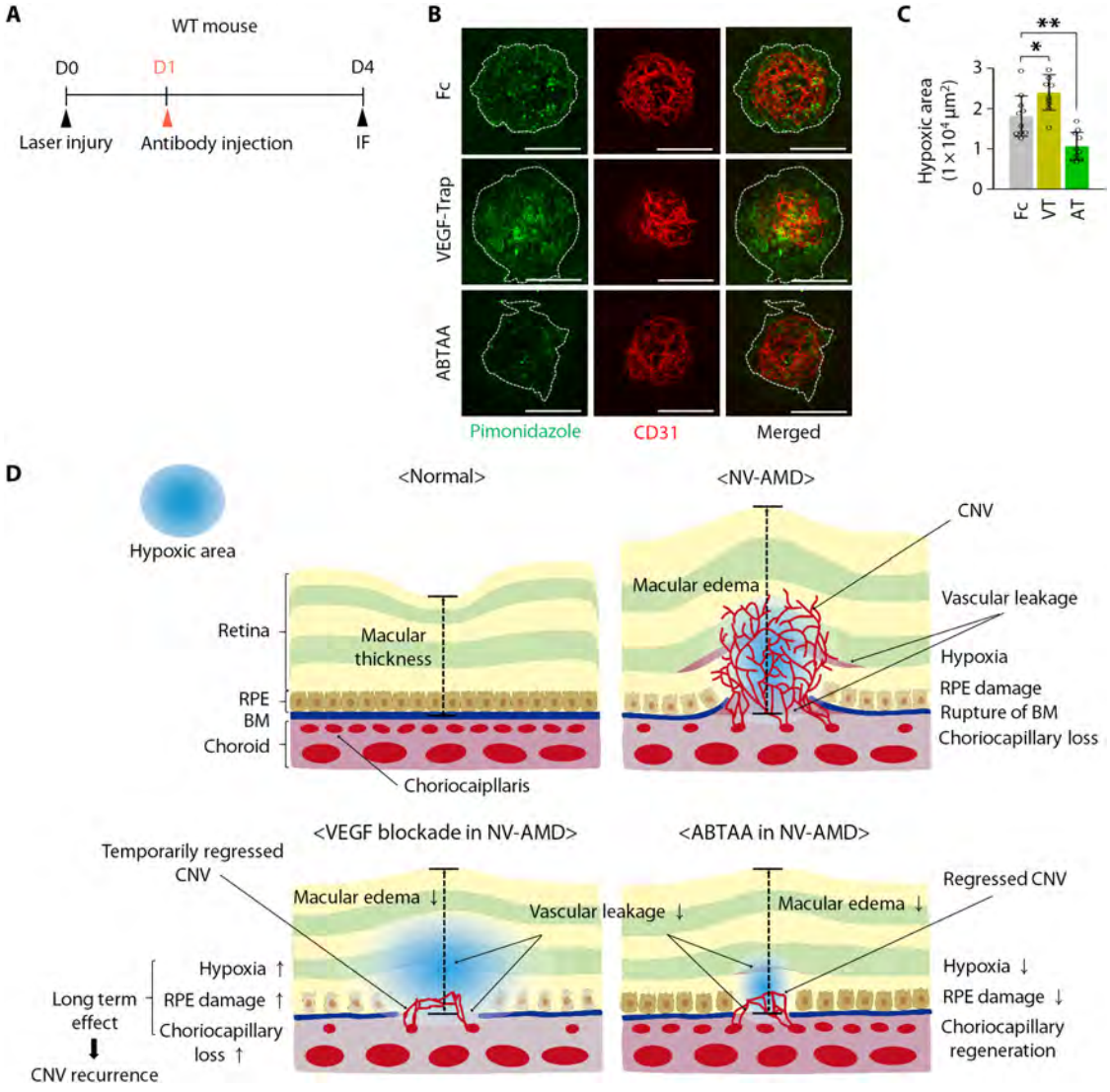

Fig. 6. ABTAA reduces hypoxia in RPE-choroid complex surrounding the CNV lesions. (**A**) Diagram of schedule for induction of CNV at D0; intravitreal administration of Fc, VEGF-Trap, or ABTAA (5 μg each) at D1; and their analyses at D4. (**B**) Images of pimonidazole staining to detect hypoxia in CNV and the surrounding RPE-choroid complex (area demarcated by the white dotted boundary) at the site of laser injury. Scale bars, 100 μm. (**C**) Comparisons of pimonidazole$^+$ hypoxic areas. Error bars represent means ± SD. Each group, $n = 10$. $^*P < 0.05$, $^{**}P < 0.005$ versus Fc by one-way ANOVA followed by Student-Newman-Keuls post-test. (**D**) Schematic diagrams depicting how ABTAA functions as an alternative, combinative treatment of NV-AMD. In normal eyes, the outer retinal layers including the RPE are supplied by diffusion from the choriocapillaris. NV-AMD is featured by the development of CNV, leading to vascular leakage and macular edema. In NV-AMD, loss of choriocapillary causes hypoxia in RPE and adjacent cells, which induces the production of VEGF, a key player in leaky neovascularization. VEGF blockades, the current treatment of choice, effectively inhibit CNV and macular edema. However, because VEGF has a central role in the maintenance of choriocapillaris, VEGF blockades could aggravate the hypoxic environments by further promoting the loss of choriocapillaris and RPE damage. On the other hand, ABTAA-induced Tie2 activation not only inhibits CNV and suppresses vascular leakage but also promotes regeneration of choriocapillaris, subsequently alleviating hypoxia and leading to a favorable transition of the CNV microenvironment to prevent recurrence of NV-AMD.

and choriocapillary loss (*2*). On the other hand, emerging evidences in patients with NV-AMD and postmortem human eyes demonstrated that the area of choriocapillary loss extends beyond the margin of RPE loss (*2*, *13*, *32*), indicating that the loss and dysfunction of choriocapillaris is the main cause of NV-AMD. This leads to excessive production of VEGF-A from the relatively intact RPE cells that are exposed to extreme hypoxia, oxidative stress, and inflammation, which consequently leads to the breakdown of the blood-retinal barrier and develops CNV (*2*). In this regard, we focused on analyzing mainly the choriocapillaris because we investigated the molecules targeting the choriocapillaris, not the RPE, and the pathogenesis of NV-AMD driven by loss of the choriocapillaris. The choriocapillaris consists of a continuous layer of fenestrated, highly permeable choriocapillary ECs (*33*). Although the choroid has the largest blood flow by weight of all organs, only ~11% of choriocapillaris are ensheathed by pericytes, a key regulator of vascular stability, whereas the capillaries in other organs are ensheathed by 34 to 95% (*12*, *34*). While the sparse pericyte ensheathment may contribute to

structural plasticity of the choriocapillaris in response to physiological changes, it could also be a cause of unavoidable vulnerability and instability in response to various pathologic insults (*12*, *34*, *35*). Along with previous reports demonstrating that the decrease in choroidal blood flow by ~20% is associated with increasing risk for CNV development (*36*) and that the number of fenestrations in choriocapillary ECs is greatly decreased in eyes of human patients with AMD (*13*), the present results revealed that impaired Angpt-Tie2 signaling impedes maintenance of choriocapillary integrity, induces visual impairment, exacerbates CNV formation, and prevents choriocapillary regeneration surrounding the CNV lesions. In this regard, Tie2 activation could be a fundamental therapeutic approach for inhibiting recurrence of NV-AMD through recovery of choroidal circulation sufficient to meet the metabolic demand of the outer retina. We demonstrate that Tie2 activation through intravitreal administration of ABTAA induces choriocapillary regeneration, not to mention suppression of CNV and vascular leakage.

The mechanism for maintaining the choriocapillaris in the rodents is not well known despite its importance in the pathogenesis of NV-AMD (*2*, *13*, *14*). Although conditional knockout mouse models targeting Tie2 and Angpt1 exhibited a glaucoma phenotype (*25*), it is reasonable to conclude that the elevated IOP in these genetic mice models was not responsible for the decreased choroidal blood flow; we demonstrated that choroidal blood flow was not changed in the microbeads-induced ocular hypertension model, and an IOP of up to 50 mmHg does not affect the volume of choroidal blood flow in cases of rat or human (*37*, *38*). In addition, there have been no suitable imaging tools for definitive visualization of the choroidal vasculature and quantifiable in vivo measurements for longitudinal analysis. Conventional dye-based two-dimensional angiography has limited axial resolution and problems distinguishing vascular abnormalities within different layers. Meanwhile, confocal immunofluorescence (IF) studies suffer from blocked fluorescence due to the RPE, a highly pigmented layer that absorbs excess light, and the impossibility of longitudinal follow-up in the same subject. Compared with previous measures, our laboratory-built high-speed OCTA system has several advantages. First, use of a wavelength-swept laser centered at 1048 nm allowed enough imaging penetration depth for clear visualization of the choroidal layer. Second, a wavelength tuning range of ~94 nm provided enough axial resolution for exact quantification of the area of retinal and choroidal vessels and the volume of CNV and avascular space in mice. Third, high-speed imaging with a repetition rate of 230 kHz enabled acquisition of full volumetric scans over a sufficiently large area without significant motion artifacts by application of a subpixel motion compensation algorithm (*39*). Fourth, the shadow projection artifacts underneath the thick retinal vessels caused by rapid attenuation of the OCTA signal in depth were shaded in another color, and the voxel of the shadow artifacts was excluded from the image analyses that were conducted automatically. Last, OCTA enables longitudinal measurements that allow normalization of CNV volumes and avascular space, which can prominently reduce the number of animals required by diminishing the effect of inherent variation in CNV sizes (*40*).

Tie2 activation may provide potential therapeutic benefits for treating microvascular diseases (*15*, *18*). It not only suppresses vascular destabilization and disseminated intravascular coagulation in experimental sepsis mice models (*19*, *41*) but also induces tumor vessel normalization in multiple tumor mouse models (*20*). We and others have found that Angpt-induced Tie2 activation plays crucial roles in the formation of Schlemm's canal and maintenance of its integrity; in addition, impairment or attenuation of the Angpt-Tie2 system is implicated in congenital and primary open-angle glaucoma (*25*, *42*, *43*). Notably, Tie2 activation through ABTAA can rejuvenate the aged Schlemm's canal and reverse its regression (*25*), leading to enhanced drainage of aqueous humor outflow and reduced IOP for the fundamental treatment of primary open-angle glaucoma. Notably, a recent report (*44*) indicates that formation of the fenestrated ascending vasa recta, a specialized lymphatic hybrid vessel for urine concentration in the renal medulla, requires Angpt-Tie2 signaling. Given the extraordinarily specialized microenvironment of the renal medulla, Angpt-Tie2 signaling could be continuously required to maintain integrity of the ascending vasa recta.

Previously, several Tie2 agonists were developed to address the unmet need for treating NV-AMD. Although intravitreal COMP-Angpt1 provides benefits in NV-AMD by suppressing CNV and its vascular leakage in the NV-AMD model (*16*), it involves limitations on production, efficacy, and half-life (*19*). Subcutaneous or intravitreal administration of the specific VE-PTP inhibitor AKB-9778, which indirectly activates Tie2 by inhibition of its dephosphorylation, leads to suppression of CNV (*17*). However, AKB-9778 may also indirectly induce activation of other receptor tyrosine kinases including VEGFR2 in a context-dependent manner (*45*). Angpt2-blocking antibodies are also being developed for treating patients with pathological retinal/choroidal angiogenesis and solid tumors. Although these antibodies significantly suppress CNV (*46*), they secondarily cause hypoxia and subsequently enhance expression of VEGF and Angpt2 during pathologic angiogenesis (*47*). Thus, ABTAA offers more advantages over these agents because of its dual function of Angpt2 blockade and Tie2 activation, long-term half-life, and convenient production for clinical purposes (*19*).

Our collective evidence elucidates the essential role of the Angpt-Tie2 system in maintaining the choriocapillaris in the context of NV-AMD. The distinguishing characteristics of ABTAA of favorably altering the CNV microenvironment by regenerating the choriocapillaris make it a novel alternative, combinative therapeutic option for filling in the gaps in current anti-angiogenic therapies. Further research to demonstrate its efficacy and safety in clinical trials remains to be done.

MATERIALS AND METHODS

Study design

The primary aims of the present study were to investigate whether the Angpt-Tie2 system is essential for the maintenance of choriocapillaris during adulthood with regard to the pathogenesis of NV-AMD and to evaluate the effect of Tie2 activation in suppressing CNV and vascular leakage and regenerating choroidal vasculatures of NV-AMD. To achieve our first aim, we initially compared the TIE2 level and density of choriocapillaris between healthy young and old adults using the cadaveric donor eyes. Then, we made transgenic mouse models to deplete Tie2 or Angpt1 and analyzed their choriocapillaris, photoreceptors, and visual functions. In addition, we induced CNV in these mice by laser photocoagulation and analyzed the extent of CNV formation and the avascular space surrounding the CNV. To accomplish our second objective, mice were randomized after laser photocoagulation-induced CNV formation for antibody administration, and we intravitreally administered a Tie2-activating antibody named ABTAA in both therapeutic and preventive settings.

CNV volume, vascular leakage, and regeneration of choriocapillary vascular network were monitored, and changes in gene expression profiles in the CNV and surrounding tissues were analyzed. No statistical method was used to predetermine the sample size. Animals or samples were not randomized during experiments. Only male mice were used in adult experiments. The investigators were blinded to the genotypes of animals during experiments. The investigators performing the subsequent analyses including morphometric, functional, and biochemical analyses were blinded to the information about treatment groups.

Sampling of human choroids

Anonymous human choroid samples were obtained from the retinochoroidal layer of healthy cadaveric donor eyes (Eversight, Ann Arbor, USA) left over from corneal transplantation surgery in the Samsung Medical Center. These were exempted from a formal review of the institutional review board at the Samsung Medical Center because of the lack of patient identifiers and the intention of being otherwise discarded. The protein expression of TIE2 was examined in the choroid of these samples using IF staining.

Mice

Specific pathogen–free (SPF) C57BL/6 J mice (#000664), *Tie2-GFP* mice (#003658), and *Ubiquitin*-Cre-ER^{T2} mice (#007001) were purchased from the Jackson Laboratory. *Angpt2-EGFP* mice (Tg [*Angpt2-EGFP*] DJ90Gsat/Mmcd) were purchased from the Mutant Mouse Regional Resource Centers. *Angpt1-GFP* (*21*), *Tie2*$^{flox/flox}$ (*22*), and *Angpt1*$^{flox/flox}$ (*27*) mice were transferred and bred in our SPF animal facilities at Korea Advanced Institute of Science and Technology (KAIST). *VE-cadherin*-Cre-ER^{T2} mice (*23*) were mated with *Tie2*$^{flox/flox}$ mice to obtain EC-specific *Tie2*-deleted mice in a tamoxifen-dependent manner. To deplete *Angpt1* globally, *Angpt1*$^{flox/flox}$ mice were crossed with *Ubiquitin*-Cre-ER^{T2} mice. Two milligrams of tamoxifen (T5648, Sigma-Aldrich) was injected intraperitoneally a total of three times every 2 days to 8-week-old genetically modified mice. All mice were fed with free access to a standard diet (PMI LabDiet) and water. All mice were anesthetized by an intramuscular injection of ketamine (40 mg/kg) and xylazine (12 mg/kg) before any procedures. All animal care and experimental procedures were carried out in accordance with the protocol approved by the Institutional Animal Care and Use Committee of KAIST (no. KA2015-15), and mice were handled according to the Association for Research in Vision and Ophthalmology Statement for the Use of Animals in Ophthalmic and Vision Research.

PCR to genotype for photoreceptor degeneration mutations

For DNA extraction, tail tissue was heated in 200 μl of chelex reagent (10% chelex, 0.1% Tween 20, and 1% proteinase K) for over 3 hours at 65°C, followed by proteinase K inactivation for 15 min at 75°C. For the polymerase chain reaction (PCR) reaction, 4 μl of the supernatant was placed into 16 μl of reaction mixture consisting of the AccuPower Taq PCR Master Mix (K-2609; Bionner) and forward and reverse primers (Macrogen). The DNA of *cng3*, *abca4*, and *pde6b* genes was amplified by PCR, and WT and mutant bands were detected as previously described (*48*, *49*).

Laser-induced CNV mouse model

Generation of the laser-induced CNV mouse model was performed according to a previously described method (*28*) with some modifications (*16*). Approximately 8-week-old male mice were used for generation of CNV. After dilating pupils with phenylephrine (5 mg/ml) and tropicamide eye drops (5 mg/ml; Santen Pharmaceutical) and instillation with 0.5% proparacaine hydrochloride eye drops (Alcon) for topical anesthesia, laser photocoagulator (Lumenis Inc.) with a slit lamp delivery system was used with a glass coverslip as a contact lens to visualize the retina. Sufficient laser energy (wavelength, 532 nm; power, 250 mW; duration, 100 ms; spot size, 50 μm) was delivered to four locations for each eye (the 3, 6, 9, and 12 o'clock positions of the posterior pole). Only burns that produced a bubble at the time of laser photocoagulation, indicating the rupture of the Bruch's membrane, were included in this study. Spots containing hemorrhage at the laser site were excluded from the analysis.

ELISA for Angpt2 in vitreal fluid of mouse

Vitreous fluid in mouse eye was sampled using the Nanoliter 2000 microinjector (World Precision Instruments) fitted with a glass capillary pipette. The concentration of Angpt2 in the vitreal fluid was measured using a mouse/rat Angpt2 enzyme-linked immunosorbent assay (ELISA) kit (R&D Systems) according to the manufacturer's instructions, and the optical density was measured using a Spectra MAX340 plate reader (Molecular Devices).

Intravitreal administration

To intravitreally administer indicated reagents, ~1 μl containing 5 μg of each reagent was injected into the vitreal cavity using the Nanoliter 2000 microinjector fitted with a glass capillary pipette.

Confocal scanning laser FA and ICGA

Using our custom-built confocal scanning laser retinal angiography system (*50*), in vivo fundus FA and ICGA of the CNV lesion were performed. Continuous-wave laser modules at 488 and 785 nm were used as excitation sources for fluorescein and ICG, respectively. A raster-scanning pattern of excitation lasers was achieved by a scanner system consisting of a rotating polygonal mirror (MC-5; Lincoln Laser) and a galvanometer-based scanning mirror (6230H; Cambridge Technology) and delivered to the back aperture of an imaging lens. A high–numerical aperture (NA) objective lens (PlanApo λ, NA 0.75; Nikon) was used as the imaging lens to provide wide-field fundus fluorescence images. Fluorescence signals detected by photomultiplier tubes (R9110; Hamamatsu Photonics) were digitized by a frame grabber and reconstructed to images with a size of 512 × 512 pixels per frame in real time. To visualize late-phase (6 min) FA and ICGA images using the angiography system, 10 mg of fluorescein sodium (Alcon) and 0.15 mg of ICG (Daiichi Pharmaceutical) were administered intraperitoneally and intravenously, respectively. The imaging procedure was performed under systemic anesthesia and pupil dilation to improve the quality of images. Leaky areas from CNV were calculated as the total measured hyperfluorescent areas in FA images divided by the total measured CNV areas in ICGA images using a Java-based imaging software (ImajeJ, NIH; available at http://rsb.info.nih.gov/ij).

Histological and morphometric analyses

IF analyses of the RPE-choroid-sclera flat mounts were performed as previously described (*16*). Enucleated eyes were fixed with 4% paraformaldehyde for 30 min at room temperature (RT). For IF staining of sectioned retina and choroid, fixed eyeballs were then dehydrated in 20% sucrose solution overnight, embedded in tissue-freezing

medium (Leica), and cut into 20-μm sections. Samples were blocked with 5% donkey or goat serum in PBST (0.3% Triton X-100 in phosphate-buffered saline) and then incubated in blocking solution with one or more of the following antibodies at 4°C overnight: rabbit anti-human CD31 polyclonal antibody (#AB32457, abcam), goat anti-human Tie2 polyclonal antibody (#AF313, R&D systems), hamster anti-mouse CD31 monoclonal antibody (#MAB1398Z, clone 2H8, Millipore), goat anti-mouse Tie2 polyclonal antibody (#AF762, R&D systems), chicken anti-GFP polyclonal antibody (#AB16901, Millipore), rat anti-mouse CD144 monoclonal antibody (#740933, clone 11D4.1, BD Biosciences), rabbit anti-mouse opsin polyclonal antibody (#AB5405, Millipore), and rabbit anti-mouse rhodopsin monoclonal antibody (#27182, clone D4B9B, Cell Signaling Technology). After several washes, the samples were incubated for 4 hours at RT with the following secondary antibodies (Jackson ImmunoResearch Laboratories): fluorescein isothiocyanate (FITC)– or Cy5-conjugated anti-hamster immunoglobulin G (IgG), FITC- or Cy3-conjugated anti-rabbit IgG, FITC- or Cy3-conjugated anti-goat IgG, FITC-conjugated anti-chicken IgG, and Cy3-conjugated anti-human IgG. Samples were mounted with fluorescent mounting medium (VectaShield H-1000; Vector Laboratories), and IF images were acquired with a confocal microscope (LSM880; Carl Zeiss Microscopy). $CD31^+$ CNV volumes were measured using the MATLAB image processing toolbox (MATLAB 8.1; MathWorks), which are presented in cubic micrometers. The volume of CNV in one eye was averaged to give one experimental value. Morphometric analyses of choriocapillaris were performed using ImageJ software (NIH). The relative area of choriocapillaris was calculated as a percentage of the $CD31^+$ area divided by its control area. To quantify the expression of Tie2 and CD144, intensities were measured in the $CD31^+$ choriocapillary area. To perform IF staining for hypoxia, mice were intraperitoneally injected with pimonidazole hydrochloride (60 mg/kg) in PBS (Hypoxyprobe Green Kit; Hypoxyprobe) and sacrificed after 1 hour. An FITC-conjugated monoclonal antibody against pimonidazole was used for IF staining of the flat-mounted RPE-choroid-sclera complex. For statistical analysis, values from four random spots at the center of the choroid in each eye were averaged. For comparison of staining intensities, the values were normalized by the background signals in nonvascularized regions, and their ratios were normalized by control and presented as percentages.

Optical coherence tomography angiography

The retino-choroidal layers were imaged using a prototype high-speed swept-source optical coherence tomography (OCT) system (*40*), using a custom ring cavity wavelength-swept laser centered at 1048 nm with an A-scan rate of 230 kHz. OCT images were collected in a 1.7 mm by 1.7 mm field of view within the retino-choroidal layer to monitor regeneration of choroidal vasculatures at the site of laser photocoagulation after intravitreal injection of reagents. To obtain cross-sectional OCT angiograms, which allows for selective visualization of blood vessels without the retinal and choroidal parenchyma, we compared repeatedly recorded B-scan images and detected pixel-by-pixel intensity decorrelation of those images that are mainly caused by movement of erythrocytes inside the vessels. Then, by using automatic layer flattening and segmentation algorithms, cross-sectional OCT angiograms were flattened to the RPE, and en face OCT angiograms were generated by separate projection of each flattened cross-sectional OCT angiogram in three depth ranges: inner retinal, outer retinal, and choroidal layers (fig. S2). The outer plexiform layer and Bruch's membrane were defined as the boundaries separating inner retinal, outer retinal, and choroidal layers. Shadow artifacts caused by relatively thick retinal vessels in the outer retina and choroid were removed in figures for better comparison. Unremoved shadow artifacts caused by major arterioles and venules in the inner retina were shaded in blue. The density of retina and choroid vessel was automatically calculated as the proportion of measured area occupied by flowing blood vessels defined as pixels having decorrelation values above the threshold level. Avascular pixels were detected from the en face OCT angiogram representing choroidal layers by means of the image processing toolbox of a commercial software (MATLAB 8.1; MathWorks). Then, the total avascular volume surrounding the laser injury site was calculated by summing the number of avascular pixels multiplied by the volume of one pixel. To analyze the changing complexion of avascular volume, serially measured values in each eye were transformed into percentage change from baseline value.

Microbeads-induced ocular hypertension mouse model

The microbeads-induced ocular hypertension mouse model was generated according to a previously described method (*51*) with some modifications. Approximately 8-week-old male mice were used. Sterilized microbeads (Polybead Microspheres; bead diameter, 1 + 6 μm; Polysciences Inc.) in 100% ethanol were washed and resuspended in PBS. After topical anesthesis by instillation with 0.5% proparacaine hydrochloride eye drops, ~4 μl containing 2 μl of equal volume mixture of two-sized microbeads (3×10^6 beads/μl for 6 μm beads and 1.5×10^7 beads/μl for 1 μm beads) and 2 μl of viscoelastic solution [sodium hyaluronate (18 mg/ml), Megacrom; Woojeon Co. Ltd] was injected into the anterior chamber using the Nanoliter 2000 microinjector fitted with a glass capillary pipette. Because the viscoelastic solution entered last into the anterior chamber and pushed microbeads into the peripheral anterior chamber, reflux of microbeads was prevented after withdrawal of the glass capillary pipette. IOP measurements were performed with a rebound tonometer (Tonolab; Tiolat), as previously described (*25*).

Electroretinogram

To assess the retinal neuronal function at indicated time points, a full-field electroretinogram was recorded in the indicated mice using Phoenix Micron IV system (Phoenix Research Labs). Mice were dark- or light-adapted for 12 hours before electroretinogram monitoring, anesthetized, and placed on a heating pad to maintain body temperature. After pupil dilatation by one-time topical application of a 0.5% tropicamide/0.5% phenylephrine mixed eye drop (Mydrin-P, Santen, Osaka, Japan), the cornea was located by gold-plated objective lens, and silver-embedded needle electrodes were located at the forehead (reference) and tail (ground). Using LabScribeERG software (Version 3, Phoenix Research Labs), the stimulus and recording of electroretinogram were performed according to the manufacturer's instruction. In the dark-adapted condition (scotopic), rod and mixed cone/rod responses to a series of white flashes of increasing intensities ranging from −2.2 to 2.2 log ($cd \cdot s/m^2$) with a digital bandpass filter ranging from 0.3 to 1000 Hz were recorded. In the light-adapted condition (photopic) with 1.3 log ($cd \cdot s/m^2$) background, cone responses to a 1-Hz stimulus ranging from 0.4 to 2.2 log ($cd \cdot s/m^2$) with the filter ranging from 2 to 200 Hz were recorded. After averaging the signals, the amplitude was presented by the LabScribeERG software and used for analyses.

Immunoblot analysis

For protein extraction, harvested retinas of both eyes in each mouse were washed with PBS containing protease inhibitor cocktail (Roche). Tissues were then homogenized with Precellysis Tissue Homogenizer (Bertin Instruments) in radioimmunoprecipitation assay buffer (Thermo Fisher Scientific) supplemented with DNase I (Roche) and protease inhibitor cocktail (Roche). Homogenized samples were centrifuged at 15,000 rpm for 20 min at 4°C. Tissue lysate soups were then subjected to SDS–polyacrylamide gel electrophoresis (PAGE). After electrophoresis, proteins were transferred to nitrocellulose membranes. After being blocked for 1 hour with 5% bovine serum albumin (BSA) in TBST (0.1% Tween 20 in tris-buffered saline), the membranes were incubated with the following antibodies at 4°C overnight: anti-Tie2 (rabbit polyclonal, catalog no. sc-324, Santa Cruz Biotechnology), anti-opsin (chicken polyclonal, catalog no. PA1-9517, Thermo Fisher Scientific), anti-rhodopsin (mouse monoclonal, clone 1D4, catalog no. ab5417, abcam), and anti-GAPDH (glyceraldehyde-3-phosphate dehydrogenase; rabbit monoclonal, clone D16H11, catalog no. 5174, Cell Signaling Technology). After washes, membranes were incubated with secondary peroxidase-coupled antibody at RT for 1 hour. Chemiluminescent signals were developed using ECL Western blot detection solution (Millipore). Resultant bands from four independent experiments were detected with a luminescent image analyzer (LAS-1000 mini, Fujifilm), and densitometry quantifications of indicated proteins normalized to GAPDH in each lane were compared using ImageJ software (NIH).

Generation of a new version of ABTAA

We generated an advanced version of ABTAA, which recognizes the different epitope of human ANGPT2 and has a higher production rate in the mammalian cells. The properties of the new version of ABTAA were almost similar to the original version of ABTAA (*19*). The new version binds to human ANGPT2 with an equilibrium dissociation constant (K_d) value of 0.9 nM (fig. S10A). Furthermore, in the presence of ANGPT2 in primarily cultured human umbilical vein ECs (HUVECs; Lonza), the ABTAA triggered TIE2 phosphorylation and activation of its downstream signals, including Akt and extracellular signal–regulated kinase (ERK), in a dose-dependent manner (fig. S10B). ABTAA + ANGPT2 also induced TIE2 translocation to cell-cell junction and nuclear clearance of FOXO1 in common with ANGPT1 (fig. S10, C and D).

Surface plasmon resonance

Surface plasmon resonance analyses were run using a Biacore T200 (GE Healthcare) instrument. Amine-coupling chemistry was used to immobilize anti-human IgG (Fc) antibody on the surface of a CM5 biosensor chip. Anti-human IgG (Fc) antibody in sodium acetate (pH 5.0) was injected over 6 min using a flow rate of 10 μl/min and gave a surface density of ~11,000 resonance units (RU). Flow cells were activated with a 1:1 mixture of 1-ethyl-3-(3-dimethylaminopropyl) carbodiimide hydrochloride and *N*-hydroxysuccinimide. Surfaces were then blocked by an injection of 1 M ethanolamine-HCl (pH 8.5). ABTAA was injected at a flow rate of 5 μl/min over 1 min and gave a surface density of 220 to 240 RU. A series of concentrations of human ANGPT2 full-length in HBS-EP buffer (10 mM HEPES, pH 7.4, 500 mM NaCl, 3 mM EDTA, 0.005% surfactant P20) were injected at a flow rate of 30 μl/min. The experiment was performed at 25°C with an association time of 4 min and a dissociation time of 3 min. After each binding cycle, a regeneration solution (3 M $MgCl_2$) was injected for 30 s at a flow rate of 30 μl/min to remove any noncovalently bound protein. Signal detection was at a rate of 10 signals/s. Data were evaluated using 1:1 binding model of BIAevaluation software version 1.0.

Immunoprecipitation and immunoblot analysis

HUVECs were purchased from Lonza. The cells were confirmed to be mycoplasma-negative (MycoAlert Detection Kit, Lonza), cultured in endothelial growth medium (EGM2-MV, Lonza), and incubated in a humidified atmosphere of 5% CO_2 at 37°C. For TIE2 immunoprecipitation, HUVECs were seeded into 100-mm culture dishes and grown to confluence. HUVECs were starved for 6 hours and then incubated with human ANGPT2 (1 μg/ml; R&D Systems) in the presence of ABTAA for 30 min. Cells were rinsed once with cold PBS and lysed in cold complete lysis-M buffer (Roche) containing protease and phosphatase inhibitors (Roche). The lysates were centrifuged at 14,000 g at 4°C for 15 min, and supernatants were subjected to immunoprecipitation with anti-TIE2 antibody (R&D systems). The immunoprecipitates were incubated with 20 μl of Dynabeads Protein G (Life Technologies) for 2 hours. Beads with immunoprecipitates were washed three times with cold lysis buffer, heated in Laemmli sample buffer at 95°C for 5 min, subjected to SDS-PAGE on 4 to 15% Mini-PROTEAN TGX Precast Gels (Bio-Rad), transferred to nitrocellulose membrane (Invitrogen), and probed with horseradish peroxidase (HRP)–conjugated anti–phosphotyrosine 4G10 antibody (Millipore). The blots were developed using the ECL Western blotting detection kit (GE Healthcare) and visualized with Amersham Imager 600 (GE Healthcare). The membranes were stripped and reprobed with an anti-TIE2 (Millipore) antibody. The primary antibodies for pAKT (S473), AKT, pERK (T202/Y204), and ERK (all from Cell Signaling) were used. Secondary HRP-conjugated antibodies (Bio-Rad) were used for signal detection.

IF staining for cultured ECs

Cells on an eight-well Lab-Tek II chamber (Nunc) were fixed with 4% formaldehyde in PBS at RT for 10 min, permeabilized with 0.1% Triton X-100 in PBS, blocked with 1% BSA in PBS at RT for 1 hour, and incubated with primary antibodies at RT for 1 hour. Primary antibodies for FOXO1 (Cell Signaling) and TIE2 (R&D Systems) were used. The cells were then incubated with secondary antibodies (Invitrogen) in the dark at RT for 1 hour and mounted with VECTASHIELD mounting medium with 4′,6-diamidino-2-phenylindole (Vector Labs). Images were taken with a confocal laser scanning microscope (LSM880, Carl Zeiss).

Laser capture microdissection

The RPE-choroidal complex was obtained from enucleated eyes and flat-mounted on polyethylene naphthalate membrane (Carl Zeiss). CNV and surrounding tissues (twofold larger in diameter than CNV itself), including the RPE and choroid, were collected using laser capture microdissection (PALM MicroBeam, Carl Zeiss) and subjected to RNA isolation.

RNA isolation, library preparation, and RNA-seq

For RNA isolation, CNV and surrounding tissues of eyes treated with Fc, VEGF-Trap, and ABTAA were used. Total RNA was isolated using TRIzol reagent (Invitrogen). RNA quality was assessed by an Agilent 2100 bioanalyzer using the RNA 6000 Nano Chip (Agilent Technologies), and RNA quantification was performed using the ND-2000 Spectrophotometer (Thermo Fisher Scientific). For library

preparation, the SENSE 3′ mRNA-seq Library Prep Kit (Lexogen Inc.) were used according to the manufacturer's instructions. Briefly, each 500 ng of total RNA was prepared, oligothymidilate primers containing an Illumina-compatible sequence at the 5′ end were hybridized to the RNA, and reverse transcription was performed. After degradation of the RNA template, second-strand synthesis was initiated by a random primer containing an Illumina-compatible linker sequence at its 5′ end. The double-stranded library was purified by using magnetic beads to remove all reaction components. The library was amplified to add the complete adapter sequences required for cluster generation. The finished library was purified of PCR components. High-throughput sequencing was performed as single-end 75 sequencing using NextSeq 500 (Illumina Inc.). For RNA-seq, the SENSE 3′ mRNA-seq reads were aligned using Bowtie2 version 2.1.0 (*52*). Bowtie2 indices were either generated from genome assembly sequence or representative transcript sequences for alignment to the genome and transcriptome. The alignment file was used to assemble transcripts, estimate their abundances, and detect differential expression of genes. DEG was determined on the basis of counts from unique and multiple alignments using EdgeR within R version 3.2.2 (R development Core Team) using BIOCONDUCTOR version 3.0 (*53*). The RT (read count) data were processed on the basis of Quantile normalization method using the Genowiz version 4.0.5.6 (Ocimum Biosolutions).

Data analysis for RNA-seq

Three biological replicates of each condition were used for analysis. Each raw count value was normalized (log 2) and then analyzed by a *P* value of less than 0.05 to determine DEGs in VEGF-Trap– and ABTAA-treated groups relative to Fc-treated group. These normalized count values were used to generate heatmaps and perform bioinformatics analysis. RNA-seq gene expression heatmap was generated with DEGs ($P < 0.05$) between VEGF-Trap– and ABTAA-treated groups using Cluster and TreeView from the Eisen laboratory (*54*). Then, we used protein annotations in Gene Ontology (GO) ID:0001666, "response to hypoxia," to generate a heatmap of hypoxia signature genes, which were plotted using Multiple Experiment Viewer from The Institute of Genomic Research. For GSEA, a gene set (KIM_HYPOXIA) from the Molecular Signatures Database 5.2 (www.broadinstitute.org/gsea/msigdb/) was used for the analysis of hypoxia-responsive transcriptomes. To compare biological effects and disease pathway outcomes of ABTAA treatment to CNV against VEGF-Trap, the set of DEGs was subjected to IPA (Qiagen). For IPA analysis, down-regulated DEGs in the VEGF-Trap–treated group and all DEGs in the ABTAA-treated group were used. Significance of the disease and biological functional terms were tested by the Fisher's exact test *P* value between DEGs and IPA knowledge base, and the activation or inhibition state of each term was determined by the activation *z*-score. The activation *z*-score reflects the fold change of DEGs, which is calculated by dividing the average of normalized count values of VEGF-Trap– and ABTAA-treated groups by that of Fc-treated group. To generate bar graphs, normalized *P* values ($-\log_{10}$) were scaled in either negative or positive values according to their activation *z*-scores. The *P* values, activation scores, and gene sets are indicated in table S1.

Statistical analyses

Plotted values are shown as means ± SD throughout this study. Statistical comparisons were performed using R 3.3.0 (The R Foundation for Statistical Computing). Indicated *P* values were obtained using one-way analysis of variance (ANOVA) followed by Student-Newman-Keuls multiple comparisons for post hoc test, paired Student's *t* test, or Mann-Whitney *U* test.

SUPPLEMENTARY MATERIALS

Supplementary material for this article is available at http://advances.sciencemag.org/cgi/content/full/5/2/eaau6732/DC1

Fig. S1. Expressions of Tie2 and Angpt1 in the RPE-choroid complex.
Fig. S2. Generation of en face OCT angiograms for measurement of retinal and choroidal blood flow.
Fig. S3. Elevated IOP is not responsible for reduced choroidal blood flow.
Fig. S4. Global *Angpt1* deletion in adult mice causes damage and loss of choriocapillaris.
Fig. S5. Loss of cone but not of rod photoreceptor in the eyes of global *Angpt1*-depleted mice.
Fig. S6. ABTAA promotes regeneration of choriocapillaris surrounding the site of laser photocoagulation in the prevention phase.
Fig. S7. ABTAA forms the Angpt2-Tie2-ABTAA complex in the mouse CNV model.
Fig. S8. Analyses of the effects of ABTAA treatment in adult *Tie2*-depleted mice.
Fig. S9. RNA-seq analysis of CNV lesions and surrounding tissues treated with VEGF-Trap and ABTAA.
Fig. S10. ABTAA binds to ANGPT2 and activates TIE2 and its downstream effectors.
Table S1. List of disease and biological function signatures identified by IPA in the CNV lesions and the surrounding RPE-choroid complex treated with VEGF-Trap or ABTAA, related to fig. S9 (E and F).

REFERENCES AND NOTES

1. Y.-C. Tham, X. Li, T. Y. Wong, H. A. Quigley, T. Aung, C.-Y. Cheng, Global prevalence of glaucoma and projections of glaucoma burden through 2040: A systematic review and meta-analysis. *Ophthalmology* **121**, 2081–2090 (2014).
2. I. Bhutto, G. Lutty, Understanding age-related macular degeneration (AMD): Relationships between the photoreceptor/retinal pigment epithelium/Bruch's membrane/choriocapillaris complex. *Mol. Aspects Med.* **33**, 295–317 (2012).
3. L. S. Lim, P. Mitchell, J. M. Seddon, F. G. Holz, T. Y. Wong, Age-related macular degeneration. *Lancet* **379**, 1728–1738 (2012).
4. F. G. Holz, S. Schmitz-Valckenberg, M. Fleckenstein, Recent developments in the treatment of age-related macular degeneration. *J. Clin. Invest.* **124**, 1430–1438 (2014).
5. Comparison of Age-related Macular Degeneration Treatments Trials (CATT) Research Group, M. G. Maguire, D. F. Martin, G. S. Ying, G. J. Jaffe, E. Daniel, J. E. Grunwald, C. A. Toth, F. L. Ferris III, S. L. Fine, Five-year outcomes with anti-vascular endothelial growth factor treatment of neovascular age-related macular degeneration: The comparison of age-related macular degeneration treatments trials. *Ophthalmology* **123**, 1751–1761 (2016).
6. M. C. Peden, I. J. Suñer, M. E. Hammer, W. S. Grizzard, Long-term outcomes in eyes receiving fixed-interval dosing of anti–vascular endothelial growth factor agents for wet age-related macular degeneration. *Ophthalmology* **122**, 803–808 (2015).
7. D. Long, Y. Kanan, J. Shen, S. F. Hackett, Y. Liu, Z. Hafiz, M. Khan, L. Lu, P. A. Campochiaro, VEGF/VEGFR2 blockade does not cause retinal atrophy in AMD-relevant models. *JCI Insight* **3**, e120231 (2018).
8. M. Young, L. Chui, N. Fallah, C. Or, A. B. Merkur, A. W. Kirker, D. A. Albiani, F. Forooghian, Exacerbation of choroidal and retinal pigment epithelial atrophy after anti–vascular endothelial growth factor treatment in neovascular age-related macular degeneration. *Retina* **34**, 1308–1315 (2014).
9. J. E. Grunwald, E. Daniel, J. Huang, G.-s. Ying, M. G. Maguire, C. A. Toth, G. J. Jaffe, S. L. Fine, B. Blodi, M. L. Klein, A. A. Martin, S. A. Hagstrom, D. F. Martin; CATT Research Group, Risk of geographic atrophy in the comparison of age-related macular degeneration treatments trials. *Ophthalmology* **121**, 150–161 (2014).
10. M. Saint-Geniez, T. Kurihara, E. Sekiyama, A. E. Maldonado, P. A. D'Amore, An essential role for RPE-derived soluble VEGF in the maintenance of the choriocapillaris. *Proc. Natl. Acad. Sci. U.S.A.* **106**, 18751–18756 (2009).
11. T. Kurihara, P. D. Westenskow, S. Bravo, E. Aguilar, M. Friedlander, Targeted deletion of *Vegfa* in adult mice induces vision loss. *J. Clin. Invest.* **122**, 4213–4217 (2012).
12. H. G. Augustin, G. Y. Koh, Organotypic vasculature: From descriptive heterogeneity to functional pathophysiology. *Science* **357**, eaal2379 (2017).
13. A. Biesemeier, T. Taubitz, S. Julien, E. Yoeruek, U. Schraermeyer, Choriocapillaris breakdown precedes retinal degeneration in age-related macular degeneration. *Neurobiol. Aging* **35**, 2562–2573 (2014).
14. J. M. Seddon, D. S. McLeod, I. A. Bhutto, M. B. Villalonga, R. E. Silver, A. S. Wenick, M. M. Edwards, G. A. Lutty, Histopathological insights into choroidal vascular loss in clinically documented cases of age-related macular degeneration. *JAMA Ophthalmol.* **134**, 1272–1280 (2016).

15. H. G. Augustin, G. Y. Koh, G. Thurston, K. Alitalo, Control of vascular morphogenesis and homeostasis through the angiopoietin–Tie system. *Nat. Rev. Mol. Cell Biol.* **10**, 165–177 (2009).
16. J. Lee, D.-Y. Park, D. Y. Park, I. Park, W. Chang, Y. Nakaoka, I. Komuro, O.-J. Yoo, G. Y. Koh, Angiopoietin-1 suppresses choroidal neovascularization and vascular leakage. *Invest. Ophthalmol. Vis. Sci.* **55**, 2191–2199 (2014).
17. J. Shen, M. Frye, B. L. Lee, J. L. Reinardy, J. M. McClung, K. Ding, M. Kojima, H. Xia, C. Seidel, R. Lima e Silva, A. Dong, S. F. Hackett, J. Wang, B. W. Howard, D. Vestweber, C. D. Kontos, K. G. Peters, P. A. Campochiaro, Targeting VE-PTP activates TIE2 and stabilizes the ocular vasculature. *J. Clin. Invest.* **124**, 4564–4576 (2014).
18. G. Y. Koh, Orchestral actions of angiopoietin-1 in vascular regeneration. *Trends Mol. Med.* **19**, 31–39 (2013).
19. S. Han, S.-J. Lee, K. E. Kim, H. S. Lee, N. Oh, I. Park, E. Ko, S. J. Oh, Y.-S. Lee, D. Kim, S. Lee, D. H. Lee, K.-H. Lee, S. Y. Chae, J.-H. Lee, S.-J. Kim, H.-C. Kim, S. Kim, S. H. Kim, C. Kim, Y. Nakaoka, Y. He, H. G. Augustin, J. Hu, P. H. Song, Y.-I. Kim, P. Kim, I. Kim, G. Y. Koh, Amelioration of sepsis by TIE2 activation–induced vascular protection. *Sci. Transl. Med.* **8**, 335ra55 (2016).
20. J.-S. Park, I.-K. Kim, S. Han, I. Park, C. Kim, J. Bae, S. J. Oh, S. Lee, J. H. Kim, D.-C. Woo, Y. He, H. G. Augustin, I. Kim, D. Lee, G. Y. Koh, Normalization of tumor vessels by Tie2 activation and Ang2 inhibition enhances drug delivery and produces a favorable tumor microenvironment. *Cancer Cell* **30**, 953–967 (2016).
21. B. O. Zhou, L. Ding, S. J. Morrison, Hematopoietic stem and progenitor cells regulate the regeneration of their niche by secreting angiopoietin-1. *eLife* **4**, e05521 (2015).
22. S. Savant, S. La Porta, A. Budnik, K. Busch, J. Hu, N. Tisch, C. Korn, A. F. Valls, A. V. Benest, D. Terhardt, X. Qu, R. H. Adams, H. S. Baldwin, C. Ruiz de Almodóvar, H.-R. Rodewald, H. G. Augustin, The orphan receptor Tie1 controls angiogenesis and vascular remodeling by differentially regulating Tie2 in tip and stalk cells. *Cell Rep.* **12**, 1761–1773 (2015).
23. K. Okabe, S. Kobayashi, T. Yamada, T. Kurihara, I. Tai-Nagara, T. Miyamoto, Y.-s. Mukouyama, T. N. Sato, T. Suda, M. Ema, Y. Kubota, Neurons limit angiogenesis by titrating VEGF in retina. *Cell* **159**, 584–596 (2014).
24. D. Y. Park, J. Lee, J. Kim, K. Kim, S. Hong, S. Han, Y. Kubota, H. G. Augustin, L. Ding, J. W. Kim, H. Kim, Y. He, R. H. Adams, G. Y. Koh, Plastic roles of pericytes in the blood–retinal barrier. *Nat. Commun.* **8**, 15296 (2017).
25. J. Kim, D.-Y. Park, H. Bae, D. Y. Park, D. Kim, C.-K. Lee, S. Song, T.-Y. Chung, D. H. Lim, Y. Kubota, Y.-K. Hong, Y. He, H. G. Augustin, G. Oliver, G. Y. Koh, Impaired angiopoietin/Tie2 signaling compromises Schlemm's canal integrity and induces glaucoma. *J. Clin. Invest.* **127**, 3877–3896 (2017).
26. J. E. Morgan, J. R. Tribble, Microbead models in glaucoma. *Exp. Eye Res.* **141**, 9–14 (2015).
27. Y. Arita, Y. Nakaoka, T. Matsunaga, H. Kidoya, K. Yamamizu, Y. Arima, T. Kataoka-Hashimoto, K. Ikeoka, T. Yasui, T. Masaki, K. Yamamoto, K. Higuchi, J.-S. Park, M. Shirai, K. Nishiyama, H. Yamagishi, K. Otsu, H. Kurihara, T. Minami, K. Yamauchi-Takihara, G. Y. Koh, N. Mochizuki, N. Takakura, Y. Sakata, J. K. Yamashita, I. Komuro, Myocardium-derived angiopoietin-1 is essential for coronary vein formation in the developing heart. *Nat. Commun.* **5**, 4552 (2014).
28. V. Lambert, J. Lecomte, S. Hansen, S. Blacher, M.-L. A. Gonzalez, I. Struman, N. E. Sounni, E. Rozet, P. de Tullio, J. M. Foidart, J.-M. Rakic, A. Noel, Laser-induced choroidal neovascularization model to study age-related macular degeneration in mice. *Nat. Protoc.* **8**, 2197–2211 (2013).
29. Y. Saishin, K. Takahashi, R. Lima e Silva, D. Hylton, J. S. Rudge, S. J. Wiegand, P. A. Campochiaro, VEGF-TRAP$_{R1R2}$ suppresses choroidal neovascularization and VEGF-induced breakdown of the blood–retinal barrier. *J. Cell. Physiol.* **195**, 241–248 (2003).
30. J. T. Regula, P. Lundh von Leithner, R. Foxton, V. A. Barathi, C. M. G. Cheung, S. B. Bo Tun, Y. S. Wey, D. Iwata, M. Dostalek, J. Moelleken, K. G. Stubenrauch, E. Nogoceke, G. Widmer, P. Strassburger, M. J. Koss, C. Klein, D. T. Shima, G. Hartmann, Targeting key angiogenic pathways with a bispecific CrossMAb optimized for neovascular eye diseases. *EMBO Mol. Med.* **8**, 1265–1288 (2016).
31. J. Ambati, B. J. Fowler, Mechanisms of age-related macular degeneration. *Neuron* **75**, 26–39 (2012).
32. D. S. McLeod, R. Grebe, I. Bhutto, C. Merges, T. Baba, G. A. Lutty, Relationship between RPE and choriocapillaris in age-related macular degeneration. *Invest. Ophthalmol. Vis. Sci.* **50**, 4982–4991 (2009).
33. C. Cavallotti, B. G. Corrado, J. Feher, The human choriocapillaris: Evidence for an intrinsic regulation of the endothelium? *J. Anat.* **206**, 243–247 (2005).
34. T. Chan-Ling, M. E. Koina, J. R. McColm, J. E. Dahlstrom, E. Bean, S. Adamson, S. Yun, L. Baxter, Role of CD44$^+$ stem cells in mural cell formation in the human choroid: Evidence of vascular instability due to limited pericyte ensheathment. *Invest. Ophthalmol. Vis. Sci.* **52**, 399–410 (2011).
35. Y. Wakatsuki, A. Shinojima, A. Kawamura, M. Yuzawa, Correlation of aging and segmental choroidal thickness measurement using swept source optical coherence tomography in healthy eyes. *PLOS ONE* **10**, e0144156 (2015).
36. J. E. Grunwald, T. I. Metelitsina, J. C. Dupont, G.-S. Ying, M. G. Maguire, Reduced foveolar choroidal blood flow in eyes with increasing AMD severity. *Invest. Ophthalmol. Vis. Sci.* **46**, 1033–1038 (2005).
37. Z. Zhi, W. O. Cepurna, E. C. Johnson, J. C. Morrison, R. K. Wang, Impact of intraocular pressure on changes of blood flow in the retina, choroid, and optic nerve head in rats investigated by optical microangiography. *Biomed. Opt. Express* **3**, 2220–2233 (2012).
38. E. Polska, C. Simader, G. Weigert, A. Doelemeyer, J. Kolodjaschna, O. Scharmann, L. Schmetterer, Regulation of choroidal blood flow during combined changes in intraocular pressure and arterial blood pressure. *Invest. Ophthalmol. Vis. Sci.* **48**, 3768–3774 (2007).
39. M. Guizar-Sicairos, S. T. Thurman, J. R. Fienup, Efficient subpixel image registration algorithms. *Opt. Lett.* **33**, 156–158 (2008).
40. J. R. Park, W. Choi, H. K. Hong, Y. Kim, S. Jun Park, Y. Hwang, P. Kim, S. Joon Woo, K. Hyung Park, W.-Y. Oh, Imaging laser-induced choroidal neovascularization in the rodent retina using optical coherence tomography angiography. *Invest. Ophthalmol. Vis. Sci.* **57**, OCT331–OCT340 (2016).
41. S. J. Higgins, K. De Ceunynck, J. A. Kellum, X. Chen, X. Gu, S. A. Chaudhry, S. Schulman, T. A. Libermann, S. Lu, N. I. Shapiro, D. C. Christiani, R. Flaumenhaft, S. M. Parikh, Tie2 protects the vasculature against thrombus formation in systemic inflammation. *J. Clin. Invest.* **128**, 1471–1484 (2018).
42. B. R. Thomson, T. Souma, S. W. Tompson, T. Onay, K. Kizhatil, O. M. Siggs, L. Feng, K. N. Whisenhunt, T. L. Yanovitch, L. Kalaydjieva, D. N. Azmanov, S. Finzi, C. E. Tanna, A. W. Hewitt, D. A. Mackey, Y. S. Bradfield, E. Souzeau, S. Javadiyan, J. L. Wiggs, F. Pasutto, X. Liu, S. W. M. John, J. E. Craig, J. Jin, T. L. Young, S. E. Quaggin, Angiopoietin-1 is required for Schlemm's canal development in mice and humans. *J. Clin. Invest.* **127**, 4421–4436 (2017).
43. A. P. Khawaja, J. N. Cooke Bailey, N. J. Wareham, R. A. Scott, M. Simcoe, R. P. Igo Jr., Y. E. Song, R. Wojciechowski, C.-Y. Cheng, P. T. Khaw, L. R. Pasquale, J. L. Haines, P. J. Foster, J. L. Wiggs, C. J. Hammond, P. G. Hysi; UK Biobank Eye and Vision Consortium, NEIGHBORHOOD Consortium, Genome-wide analyses identify 68 new loci associated with intraocular pressure and improve risk prediction for primary open-angle glaucoma. *Nat. Genet.* **50**, 778–782 (2018).
44. Y. Kenig-Kozlovsky, R. P. Scott, T. Onay, I. A. Carota, B. R. Thomson, H. J. Gil, V. Ramirez, S. Yamaguchi, C. E. Tanna, S. Heinen, C. Wu, R. V. Stan, J. D. Klein, J. M. Sands, G. Oliver, S. E. Quaggin, Ascending vasa recta are angiopoietin/Tie2-dependent lymphatic-like vessels. *J. Am. Soc. Nephrol.* **29**, 1097–1107 (2018).
45. M. Hayashi, A. Majumdar, X. Li, J. Adler, Z. Sun, S. Vertuani, C. Hellberg, S. Mellberg, S. Koch, A. Dimberg, G. Y. Koh, E. Dejana, H.-G. Belting, M. Affolter, G. Thurston, L. Holmgren, D. Vestweber, L. Claesson-Welsh, VE-PTP regulates VEGFR2 activity in stalk cells to establish endothelial cell polarity and lumen formation. *Nat. Commun.* **4**, 1672 (2013).
46. M. Ratner, Next-generation AMD drugs to wed blockbusters. *Nat. Biotechnol.* **32**, 701–702 (2014).
47. R. Mazzieri, F. Pucci, D. Moi, E. Zonari, A. Ranghetti, A. Berti, L. S. Politi, B. Gentner, J. L. Brown, L. Naldini, M. De Palma, Targeting the ANG2/TIE2 axis inhibits tumor growth and metastasis by impairing angiogenesis and disabling rebounds of proangiogenic myeloid cells. *Cancer Cell* **19**, 512–526 (2011).
48. M. Biel, M. Seeliger, A. Pfeifer, K. Kohler, A. Gerstner, A. Ludwig, G. Jaissle, S. Fauser, E. Zrenner, F. Hofmann, Selective loss of cone function in mice lacking the cyclic nucleotide-gated channel CNG3. *Proc. Natl. Acad. Sci. U.S.A.* **96**, 7553–7557 (1999).
49. J. D. Blazek, C. N. Billingsley, A. Newbauer, R. J. Roper, Embryonic and not maternal trisomy causes developmental attenuation in the Ts65Dn mouse model for Down syndrome. *Dev. Dyn.* **239**, 1645–1653 (2010).
50. J. Y. Lee, Y. Hwang, J. H. Kim, Y. S. Kim, B. K. Jung, P. Kim, H. Lee, In vivo fluorescence retinal imaging following AAV2-mediated gene delivery in the rat retina. *Invest. Ophthalmol. Vis. Sci.* **57**, 3390–3396 (2016).
51. F. E. Cone, M. R. Steinhart, E. N. Oglesby, G. Kalesnykas, M. E. Pease, H. A. Quigley, The effects of anesthesia, mouse strain and age on intraocular pressure and an improved murine model of experimental glaucoma. *Exp. Eye Res.* **99**, 27–35 (2012).
52. B. Langmead, S. L. Salzberg, Fast gapped-read alignment with Bowtie 2. *Nat. Methods* **9**, 357–359 (2012).
53. R. C. Gentleman, V. J. Carey, D. M. Bates, B. Bolstad, M. Dettling, S. Dudoit, B. Ellis, L. Gautier, Y. Ge, J. Gentry, K. Hornik, T. Hothorn, W. Huber, S. Iacus, R. Irizarry, F. Leisch, C. Li, M. Maechler, A. J. Rossini, G. Sawitzki, C. Smith, G. Smyth, L. Tierney, J. Y. Yang, J. Zhang, Bioconductor: Open software development for computational biology and bioinformatics. *Genome Biol.* **5**, R80 (2004).
54. M. B. Eisen, P. T. Spellman, P. O. Brown, D. Botstein, Cluster analysis and display of genome-wide expression patterns. *Proc. Natl. Acad. Sci. U.S.A.* **95**, 14863–14868 (1998).

Acknowledgments: We thank Y. Nakaoka (Osaka University) for providing *Angpt1*$^{flox/flox}$ mice and J. Kim (Seoul National University) for assistance with statistical analysis. We dedicate this paper to G.-J. Song (The Founder of Kyung-Ahm Education and Culture Foundation) who is

suffering from NV-AMD on his heartfelt encouragement for this study. **Funding**: This study was supported by grants from the Institute for Basic Science (IBS-R025-D1-2015 to G.Y.K) funded by the Ministry of Science and ICT, Republic of Korea, from the National Research Foundation of Korea (2016M3C7A1913844 to W.-Y.O), and from the Ministry of Health and Welfare of Republic of Korea (HI15C0001 to W.-Y.O.). **Author contributions**: J.K., J.R.P., J.C., I.P., Y.H., H.B., Y.Ki., W.C., J.M.Y., and S.H. designed and performed the experiments and analyzed the data. T.-Y.C. provided the human samples and critical comments on this study. P.K. contributed intellectually to the study. Y.Ku. and H.G.A. provided the mice and critical comments on this study. J.K., J.R.P., W.-Y.O., and G.Y.K. generated the figures and wrote and edited the manuscript. W.-Y.O. and G.Y.K. directed and supervised the project. **Competing interests**: P.K., J.R.P., J.K., W.-Y.O., and G.Y.K. are inventors on a patent application related to this work filed with the Institute for Basic Science (IBS) and the Korea Advanced Institute of Science and Technology (KAIST) (no. 62/633,038, filed on 20 February 2018). The authors declare that they have no other competing interests. **Data and materials availability**: All data needed to evaluate the conclusions in the paper are present in the paper and/or the Supplementary Materials. Additional data related to this paper may be requested from the authors.

Submitted 4 July 2018
Accepted 3 January 2019
Published 13 February 2019
10.1126/sciadv.aau6732

Citation: J. Kim, J. R. Park, J. Choi, I. Park, Y. Hwang, H. Bae, Y. Kim, W. Choi, J. M. Yang, S. Han, T.-Y. Chung, P. Kim, Y. Kubota, H. G. Augustin, W.-Y. Oh, G. Y. Koh, Tie2 activation promotes choriocapillary regeneration for alleviating neovascular age-related macular degeneration. *Sci. Adv.* **5**, eaau6732 (2019).

Tie2 activation promotes choriocapillary regeneration for alleviating neovascular age-related macular degeneration

Jaeryung Kim, Jang Ryul Park, Jeongwoon Choi, Intae Park, Yoonha Hwang, Hosung Bae, Yongjoo Kim, WooJhon Choi, Jee Myung Yang, Sangyeul Han, Tae-Young Chung, Pilhan Kim, Yoshiaki Kubota, Hellmut G. Augustin, Wang-Yuhl Oh and Gou Young Koh

Sci Adv **5** (2), eaau6732.
DOI: 10.1126/sciadv.aau6732